mmWave Channel Model for Intra-Vehicular Wireless Sensor Networks

A thesis submitted in fulfilment of the requirements for

the degree of

Master of Science

in

Electrical and Electronics Engineering

KOÇ UNIVERSITY

Mertkan Koca

January 2021

Koç University

Graduate School of Science and Engineering

This is to certify that I have examined this copy of master's thesis by

Mertkan Koca

and have found it is complete and satisfactory in all respects,
and that are all revisions required by the final
examining committee have been made.

Committee:

Prof. Sinem Coleri (Advisor)

Assoc. Prof. Ertuğrul Başar

Prof. Murat Uysal

Daima arkamda olan
Annem'e ve Babam'a

Acknowledgements

I would like to express my heartfelt gratitude and respect to my advisor Prof. Sinem Çöleri for guiding me through every obstacle with everlasting faith. I am also grateful to members of my thesis committee Prof. Murat Uysal and Assoc. Prof. Ertuğrul Başar for their valuable comments during my defense.

First and foremost, I would like to present my profound love and gratitude to my parents, my sister and my niece. I consider myself as the luckiest person on earth for feeling their unconditional love at all times. I will forever be in their debt for everything they did to this day and will do from now on. Hence, I dedicate this work to them.

I also would like to express my gratitude to *Gökhan Gürbilek*, for being both a great friend and an amazing peer. It has been a pleasure having him by my side in almost every moment of this journey. We managed to get through so much together that he has become more of a brother to me rather than an ordinary friend.

Finally, I would like to thank my closest friends *Ece Işıl Ecevit, Nahit Mücellit, Eren Kaval* and *Simay Gökulu* for making my time in Koç University an unforgettable one.

Abstract

Intra-vehicular wireless sensor networks (IVWSNs) have significant potential to reduce part, manufacturing and repair costs, facilitate the integration of new nodes and provide more freedom for the sensor placement in previously impossible locations by obviating the need for wiring harness. mmWave stands up as a promising candidate to fulfill the high reliability, security and low latency requirements of IVWSNs, exploiting the availability of large bandwidth at high frequencies and high nominal gains with directional antennas. This work focuses on building the channel model for the engine compartment, passenger compartment and beneath the chassis of a vehicle by conducting vast number of measurements for 14x14, 13x13and 15x15 transmitter and receiver links in a Fiat Linea, respectively. The path loss exponent is approximately 3, showing almost no variation within different compartments. The power variation around the path loss model has a Generalized Extreme Value (GEV) distribution with zero mean for all compartments and 5 dB standard deviation for the engine compartment and approximately 7.6 dB standard deviation for the other two compartments. A modified Saleh - Valenzuela (SV) model is used to represent the clustering of power delay profiles (PDPs). Log-normal distribution is used to model the inter-arrival times of clusters, while the dependencies of cluster amplitude and ray decay rate on the cluster arrival times are represented by a dual slope linear fit model with breakpoints 1.2 ns and 5.6 ns for engine compartment, respectively, and 1.6 ns and 2.6 ns for the other two compartments, respectively. The experimental PDPs vary around the SV model and these variations are represented by a normal distribution with zero mean and 5.8 dB standard deviation, which is independent of both the delay

bins and the compartment of the vehicle. All these findings are used to build a simulation model for each compartment of the vehicle. The simulation model is validated by comparing the distributions of the received powers and Root Mean Square (RMS) delay spreads of the experimental and simulated PDPs.

Özetçe

Araç içi kablosuz sensör ağları (IVWSN'ler), kablo demeti ihtiyacını ortadan kaldırarak parça, üretim ve onarım maliyetlerini azaltma, yeni düğümlerin entegrasyonunu kolaylaştırma ve sensör yerleşimi için önceden imkansız olan yerlerde daha fazla özgürlük sağlama konusunda önemli bir potansiyele sahiptir. mmWave, IVWSN'lerin yüksek güvenilirlik, güvenlik ve düşük gecikme gereksinimlerini karşılama konusunda gelecek vaat eden bir aday olarak öne çıkıyor ve yüksek frekanslarda geniş bant genişliği ve yönlü antenlerle yüksek nominal kazançlardan yararlanıyor. Bu çalışma, bir Fiat Linea'da sırasıyla 14x14, 13x13 ve 15x15 verici ve alıcı bağlantıları için çok sayıda ölçüm gerçekleştirerek bir aracın motor bölmesi, yolcu bölmesi ve şasi altı için kanal modeli oluşturmaya odaklanmaktadır. Yol kaybı üssü yaklaşık 3'tür ve farklı bölmeler içinde neredeyse hiç değişiklik göstermez. Yol kaybı modeli etrafındaki güç değişimi, tüm bölmeler için sıfır ortalama ve motor bölmesi için 5 dB standart sapma ve diğer iki bölme için yaklaşık 7,6 dB standart sapma ile Genelleştirilmiş Uç Değer (GEV) dağılımına sahiptir. Güç gecikme profillerinin (PDP'ler) kümelenmesini temsil etmek için değiştirilmiş bir Saleh - Valenzuela (SV) modeli kullanılmıştır. Log-normal dağılım, kümelerin varış zamanlarını modellemek için kullanılırken, küme varış zamanlarına küme genliği ve ışın bozulma oranının bağımlılıkları, motor bölmesi için sırasıyla 1.2 ns ve 5.6 ns, ve diğer iki bölme için sırasıyla 1.6 ns ve 2.6 ns kesme noktalarına sahip bir çift eğimli doğrusal uyum modeli ile temsil edilir. Deneysel PDP'ler, SV modeli etrafında değişir ve bu varyasyonlar, hem gecikme bölmelerinden hem de aracın bölmesinden bağımsız olan, sıfır ortalama ve 5,8 dB standart sapma ile normal bir

dağılımla temsil edilir. Tüm bu bulgular, aracın her bölmesi için bir simülasyon modeli oluşturmak için kullanılır. Simülasyon modeli, alınan güçlerin dağılımları ile deneysel ve simüle edilmiş PDP'lerin Ortalama Karekök (RMS) gecikme yayılımları karşılaştırılarak doğrulanır.

Table of Contents

List of Figures

List of Tables

Chapter 1: Introduction

1.1 Intra-Vehicular Wireless Sensor Networks

Vehicle manufacturers tend to replace mechanical control systems with electronic counterparts in modern vehicles due to lower integration costs and design complexity [1]. These electronics systems consist of sensor networks with wired interconnections to vehicle battery for power and communication, e.g. CAN, LIN [2]. The exponential increase in the number of electronic components and corresponding wiring harnesses over the past twenty years has significantly increased the fuel consumption, design complexity and manufacturing cost of vehicles. An average car contains wiring reaching up to 4 km in length. A solution would be removing the wiring of the sensors by the use of wireless communication. This transition would also facilitate the integration of new nodes into the sensor network as well as providing more freedom in moving parts, such as tires, e.g., tire pressure sensors and Intelligent Tire [3].

1.2 mmWave

There are several candidate technologies for intra-vehicular wireless sensor networks (IVWSN), including Radio-Frequency identification (RFID) [4]–[6], ultrawideband (UWB) [7]–[14] and mmWave [15]–[17]. mmWave is considered to be one of the promising candidates with its potential to satisfy the high reliability, security and low latency requirements of IVWSN due to the availability of large bandwidth at high frequencies, high nominal gains with directional antennas and low interference with very high attenuation through the car [18]. mmWave spectrum is the extremely high frequency (EHF) band spanning 30 GHz to 300 GHz.

1.3 Related Work

Prior to building a reliable IVWSN at mmWave bands, the channel should be characterized to determine the compatibility of the technology for intended application. Wide range of mmWave channel models in the literature derived for indoor [19]–[22] and outdoor [22]–[24] channels, cannot be used for IVWSN, since vehicle compartments consist of relatively dense and unevenly distributed shadowing agents, which can occasionally act as reflectors as well. There are several studies on mmWave channel modelling in different vehicle types and various compartments, including the passenger compartment of a bus [25], passenger compartment of a car [15]–[17], [26], [27], passenger compartment of a train [28], passenger compartment of a ship [29]. However, no mmWave channel model has been proposed for the engine compartment and beneath the chassis of a vehicle. Moreover, the models proposed for the passenger compartment are based on a limited number of transmitter and receiver links, i.e. 1x9 links for [15], 1x2 links for [16], [17], 1x4 links for [26] and 4x5 links for [27]. Furthermore, none of these studies build a simulation model for the mmWave channel nor verify the validity of the model at different compartments of a vehicle.

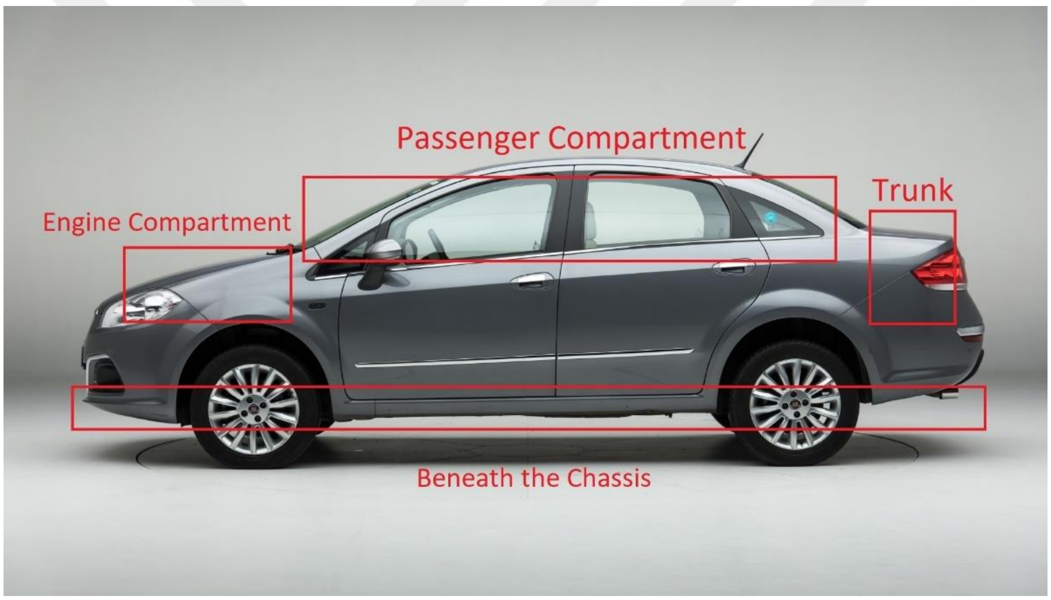

Figure 1.1: Locations that have similar propagation characteristics within.

Reference	Measurement Location	# of transmitter and receiver pairs
[15]	passenger compartment	1×9
[16]	passenger compartment	1×2
[17]	passenger compartment	1×2
[26]	passenger compartment	1×4
[27]	passenger compartment	4×5

Table 1.1: Summary of literature on intra-vehicular mmWave channel measurements

1.4 Original Contributions

The main goal of this thesis is to propose and validate a detailed simulation model for the mmWave channel within the engine compartment, passenger compartment and beneath the chassis of a vehicle. The main contributions of this work are presented below:

- We present complete mmWave channel models for engine compartment, passenger compartment and beneath the chassis of a vehicle based on the detailed analyses of the distributions, parameters and dependence relations related to the channel model, for the first time in the literature. The analyses include path loss, power variation around the expected path loss, the distributions of the interarrival times of clusters and the dependencies of cluster amplitudes and cluster decay rates on cluster arrival times in Saleh - Valenzuela (SV) Model.
- We provide the simulation models of mmwave channels based on the derived channel statistics and the validation of these models based on the comparison of root mean square (RMS) delay spread and received power of the simulation and measurement data. This is the first simulation model considering all three compartments for intra-vehicular mmWave channels.

1.5 Organization

The rest of the thesis is organized as follows. Chapter II presents the setup and the data processing to obtain the statistics. Chapter III provides the statistical channel model that include path loss model and the general shape of impulse response. Chapter

IV provides both the generation and the validation of the simulation model. Finally, the conclusive points are presented in Chapter V.

Chapter 2: System Model

2.1 Experimental Setup

Channel measurements are conducted in the frequency domain by using Rohde Schwarz ZVA67 vector network analyzer (VNA) for the frequency range of 58 - 63 GHz using 5001 points with a bandwidth of 5 GHz. The input power of the VNA is set to 10 dBm for an IF bandwidth of 1 kHz and frequency step size of 1 MHz. The mmWave antennas used for data collection are Pasternack WR-15 waveguide standard gain horn antennas operating from 50 GHz to 75 GHz with nominal 24 dBi gain with UG385/U round cover flange with waveguide to coax adapter. The dimensions of the antennas including their adapter are roughly 10 cm in length, 5 cm in width and 5 cm in height. The antennas are connected to VNA by using low-loss 1.85mm male to 1.85mm female precision cable with 48-inch length. The VNA is calibrated before each measurement for the corresponding frequency band in order to eliminate any effect from cables and connectors.

The measurements are conducted within the engine compartment, passenger compartment and beneath the chassis of a Fiat Linea MY 2009 for 182, 156 and 210 different links, respectively, as shown in Fig. 2.1. A sample measurement setup in Fiat Linea MY 2009 is given in Fig. 2.2. The engine compartment and passenger compartment measurements are conducted in the laboratory while an empty parking lot was utilized for beneath the chassis measurements. The location of the transmitters and receivers for the links are chosen as possible sensor locations. The resulting links include both line-of-sight (LoS) links with no obstacles in between and non-LOS links with obstacles blocking their sight. The antennas are always positioned in a way such that the received power attains its maximum value [30], [31]. After manually adjusting the antennas to the position where the maximum power is attained for each link, the antenna stabilization is ensured with several pipe and hose clamps to keep the azimuth angle, zenith angle and elevation steady.

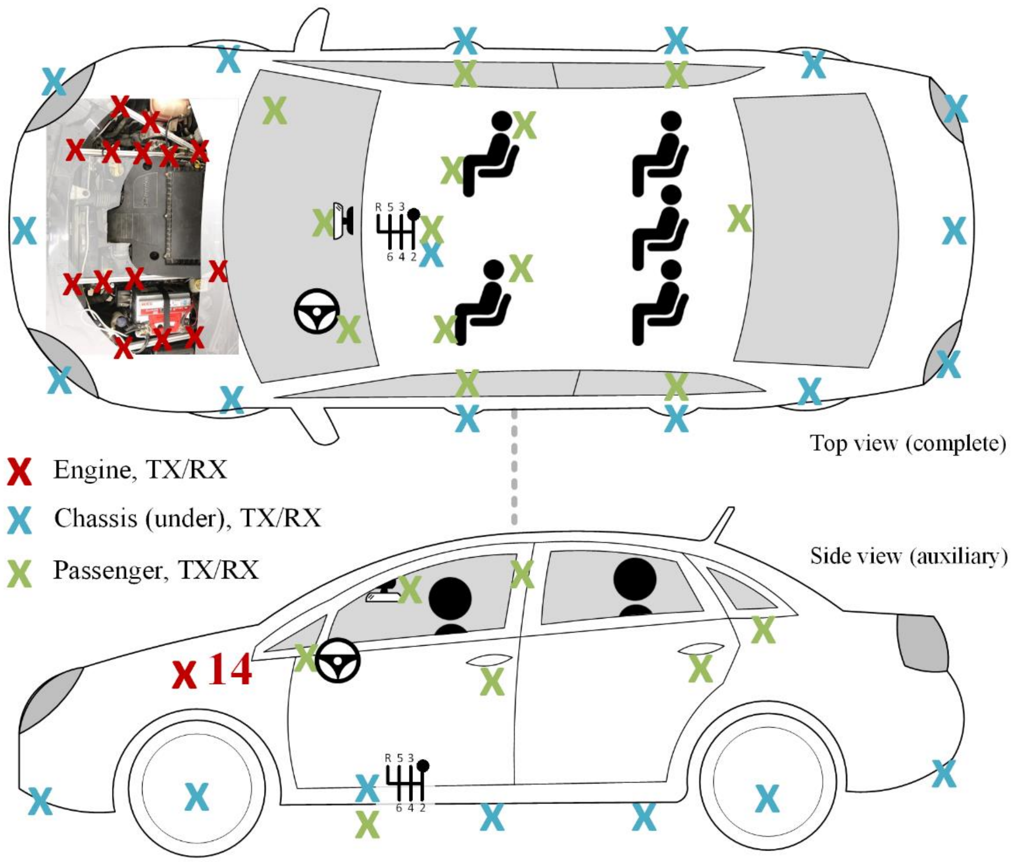

Figure 2.1: Sensor locations within each compartment of Fiat Linea MY 2009

Figure 2.2: Sample measurement setup in Fiat Linea MY 2009.

2.2 Data Processing

MATLAB R2020b is employed to carry out all of the following analyses. The output of the VNA is the Channel Frequency Response (CFR) or H(f). Path loss is calculated by finding the difference between output power and input power in dB-scale, and then subtracting the total antenna gains. The analysis of the probabilistic distributions of the inter-arrival times of clusters, cluster amplitudes and ray decay rates, requires extracting Channel Impulse Response (CIR) h(t). The VNA output H(f) is passed through Hamming window, in order to prevent spectral leakage to sidelobes while giving up in measurement resolution. The inverse Fast Fourier Transform (IFFT) of the resulting transfer function is taken to get h(t). The PDP is then given by $|h(t)|^2$. PDP is shifted to the left by propagation delay in order to align the beginning of the PDP with the first multipath component (MPC). The main objective of this work is to derive simulation models for the PDPs in each compartment and validate them.

Chapter 3: Statistical Channel Modeling

3.1 Path Loss Model

This chapter focuses on the derivations of path loss models and the distributions of the power variation of the residuals around the best fit lines for the path loss model. In vehicle compartments, the path loss between a transmitter and a receiver is not only the free space attenuation but also the attenuation in signal strength due to absorption, diffraction, reflection and refraction caused by uneven surfaces. The general path-loss model [32] is given by

$$PL_{dB}(d) = PL_{dB}(d_r) + 10n\log_{10}\left(\frac{d}{d_r}\right) + N \tag{3.1}$$

where $PL_{dB}(d)$ is the path loss at distance d, $PL_{dB}(d_r)$ is the path loss at distance $d_r = 1\ cm$, n is the path loss exponent and N is a random variable representing shadowing component. Fig. 3.1. shows the path loss as a function of distance with the best fit lines abiding Eqn. (3.1) for the engine compartment, passenger compartment and beneath the chassis of a Fiat Linea MY 2009. The best fit line for the engine compartment contains two parts: less than log-distance 1.8 and more than log-distance 1.8. The main reason for this separation is the high density of Non-LoS (NLoS) links at large distances within the engine compartment, causing the best fit line for the path loss to be very steep, resulting in a negative path loss value at reference distance. In order to have a more accurate model, we find the best fit line for the data points belonging to the distances up to 1.8. Then, for the distances larger than 1.8, we use the best fit line with the same slope but different offset.

The path loss exponents are estimated to be 2.9902, 3.0586 and 3.0067, the path loss at the reference distance is given by 25.6665, 20.8113 and 24.4302, and the standard deviation of shadowing variable are found to be 4.9917, 7.5482 and 7.7271 dB for engine compartment, passenger compartment and beneath the chassis, respectively, as shown in Table 3.1 The engine compartment is relatively smaller compared to the other two compartments, hence the variations are also smaller.

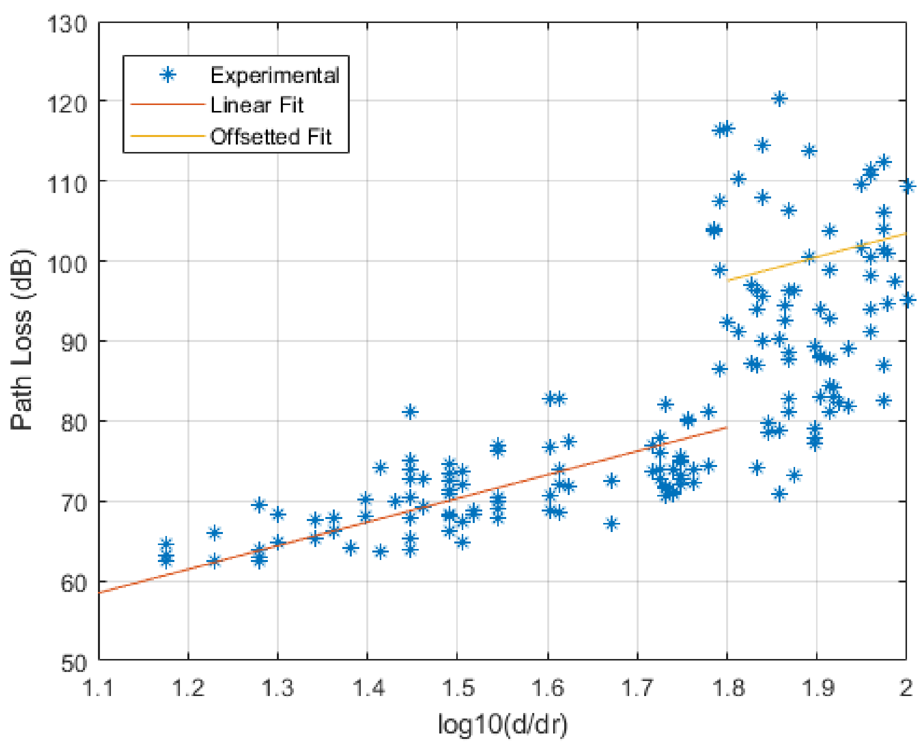

Path Loss (dB)
log10(d/dr)
Experimental
Linear Fit
Offsetted Fit
130
120
110
100
90
80
70
60
50
1.1
1.2
1.3
1.4
1.5
1.6
1.7
1.8
1.9
2

(a)

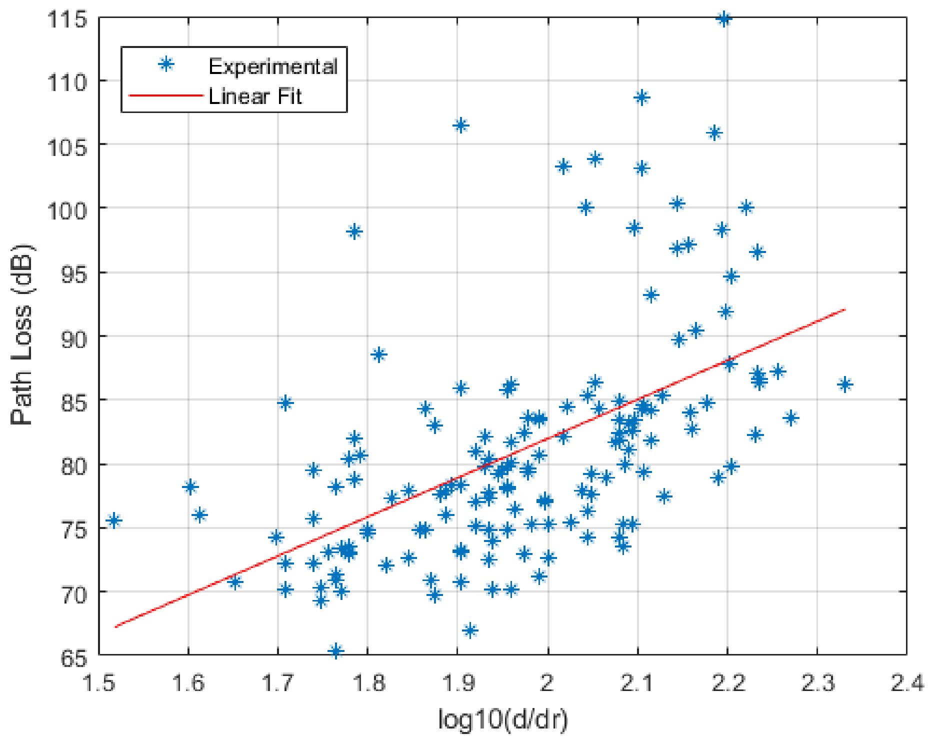
Experimental
Linear Fit
Path Loss (dB)
log10(d/dr)
115
110
105
100
95
90
85
80
75
70
65
1.5
1.6
1.7
1.8
1.9
2
2.1
2.2
2.3
2.4

(b)

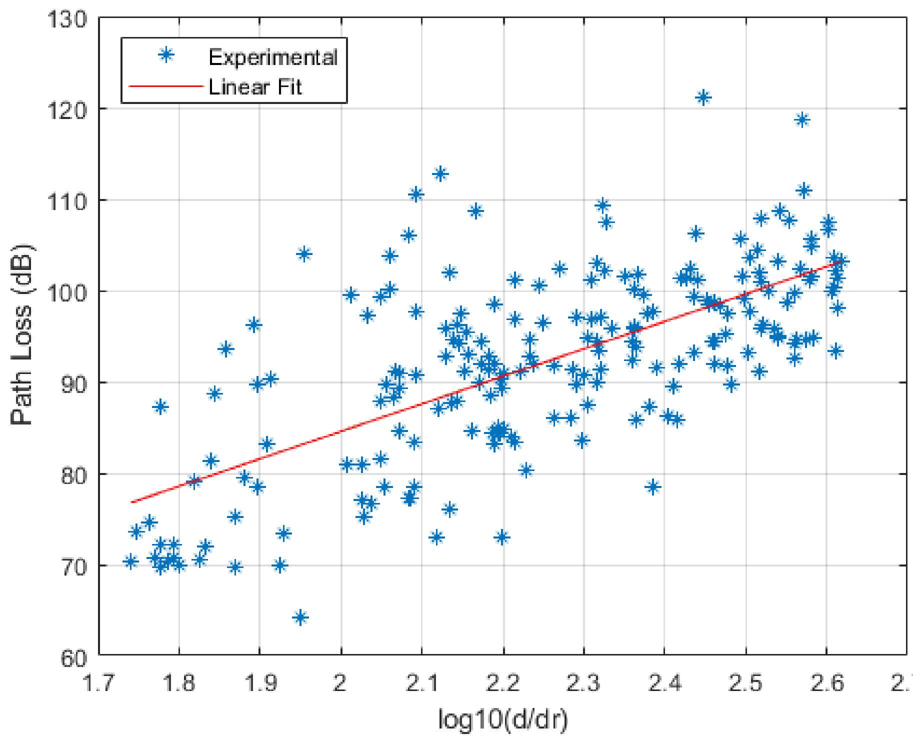

Figure 3.1: Path Loss as a function of distance with best fit lines for (a) engine compartment, (b) passenger compartment, (c) beneath the chassis.

Compartment	$\boldsymbol{n}$	$\boldsymbol{PL_{dB}(d_r)}$	$\boldsymbol{\sigma_N}$
Engine	2.9902	25.6665	4.9917
Passenger	3.0586	20.8113	7.5482
Chassis	3.0067	24.4302	7.7271

Table 3.1: Path loss parameters.

Fig. 3.2 shows the cumulative distribution function (CDF)s of the experimental power variations in terms of dB together with the Generalized Extreme Value (GEV) distribution fits for engine compartment, passenger compartment and beneath the chassis of Fiat Linea MY 2009. The experimental power variation is given by the difference between experimental path loss value and the best fit for the path loss model at the corresponding distance. Kolmogorov - Smirnov (KS) test, which is a non-parametric test to determine the goodness of a reference distribution for an experimental set of data, is employed to find the best fitting distribution. The KS test results given in Table 3.2 along with distribution parameters indicate that GEV distribution outperforms Normal distribution in all compartments. Generally, log-normal distribution is used to model the shadowing [33], however there are examples of GEV distribution in the literature for the same purpose [34], [35]. The shape parameters (k) are -0.05, 0.07 and - 0.13, the scale parameters (σ) are 4.12, 5.31 and 6.97, and the location parameters (μ) are -2.19, -3.47 and -3.17, for the engine compartment, passenger compartment and beneath the chassis, respectively. The shape parameters are very close to 0 in all compartments while the scale parameters have their fair distinction between compartments, and finally the location parameters of the passenger compartment and beneath the chassis are very similar and higher than that of the engine compartment.

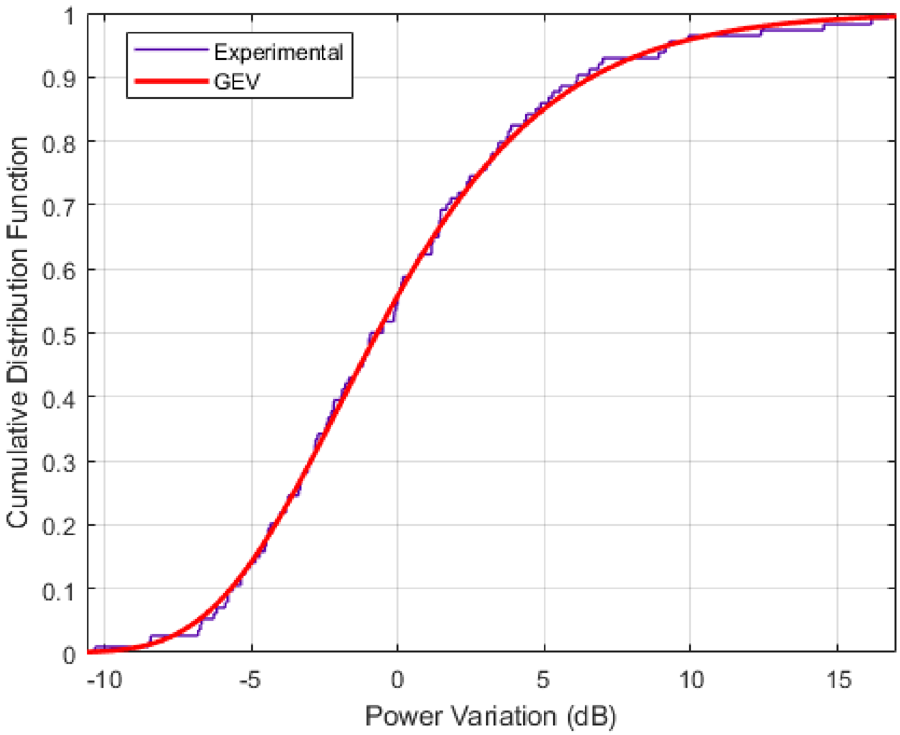

Experimental
GEV
Cumulative Distribution Function
0
0.1
0.2
0.3
0.4
0.5
0.6
0.7
0.8
0.9
1
-10
-5
0
5
10
15
Power Variation (dB)

(a)

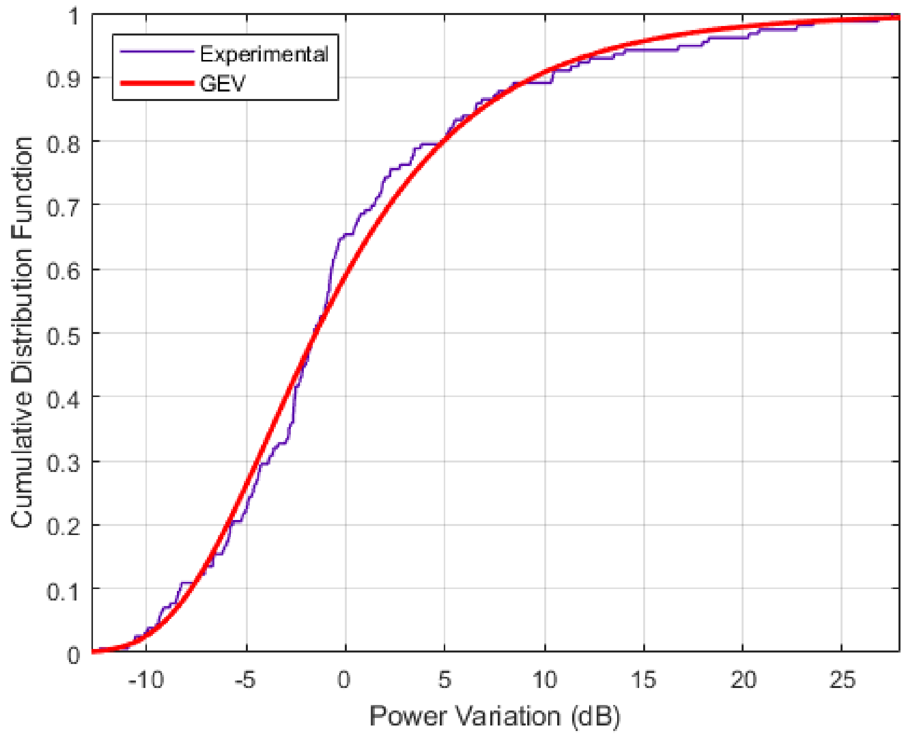

Experimental
GEV
Cumulative Distribution Function
Power Variation (dB)
0
0.1
0.2
0.3
0.4
0.5
0.6
0.7
0.8
0.9
1
-10
-5
0
5
10
15
20
25

(b)

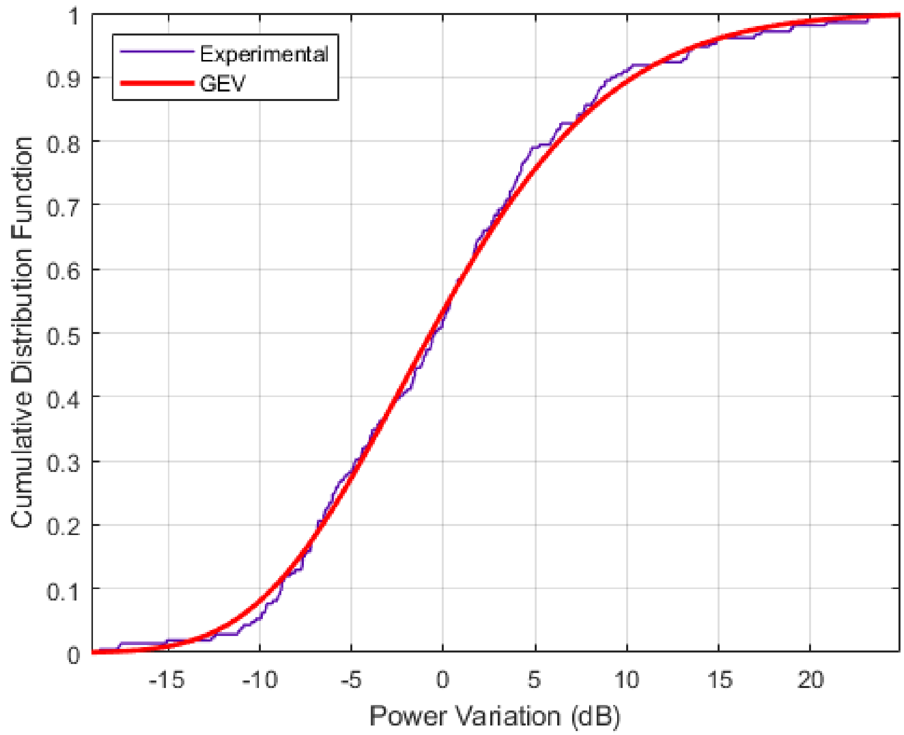

(c)

Figure 3.2: CDF of power variation for (a) engine compartment, (b) passenger compartment, (c) beneath the chassis.

Compartment	$\boldsymbol{k}$	$\boldsymbol{\sigma}$	$\boldsymbol{\mu}$	$\boldsymbol{KS_N}$	$\boldsymbol{KS_{GEV}}$
Engine	-0.0455	4.1157	-2.1938	0.0788	0.0297
Passenger	0.0711	5.3093	-3.4673	0.1634	0.0751
Chassis	-0.1340	6.9687	-3.1709	0.0571	0.0404

Table 3.2: Parameters of GEV distribution over power variation along with KS test results for Normal and GEV distributions.

3.2 General Shape of Impulse Response

The PDPs in all compartments contain clusters, as illustrated in Fig. 3.3 for a communication link in the engine compartment of Fiat Linea MY 2009. The amplitude and arrival time of clusters are modeled by using the SV model [36], which is commonly used for millimeter-wave (mmWave) channels. Impulse response in the SV model is given by

$$y(t) = \sum_{b=0}^{B}\sum_{a=0}^{A}\alpha_{b,a}e^{-j\phi_{b,a}}\sigma(t - T_b - \tau_{b,a}) \tag{3.2}$$

where A is the number of multipath components in a cluster; B is the number of clusters; $\alpha_{b,a}$ is the gain and $\phi_{b,a}$ is the phase, which is uniformly distributed in the range of [0, 2π], of the ath component of the bth cluster; T_b is the delay of the bth cluster; $\tau_{b,a}$ is the delay of the ath multipath component in the bth cluster relative to the bth cluster arrival time ; T_b.

Next, we will propose a novel clustering algorithm for the accurate identification of the clusters within the PDPs in all three compartments in Section 3.2.1. We will then continue by deriving the distribution of the inter-arrival times of clusters in Section 3.2.2, the dependence of the cluster amplitude on the cluster arrival time in Section 3.2.3 and dependence of the ray decay rate on the cluster arrival time in Section 3.2.4. Instead of analyzing the distribution of ray arrival times, a tapped delay line model with regular tap spacing is employed to mimic the rays within a cluster since we will have the overall shape of each cluster from the other three components mentioned above.

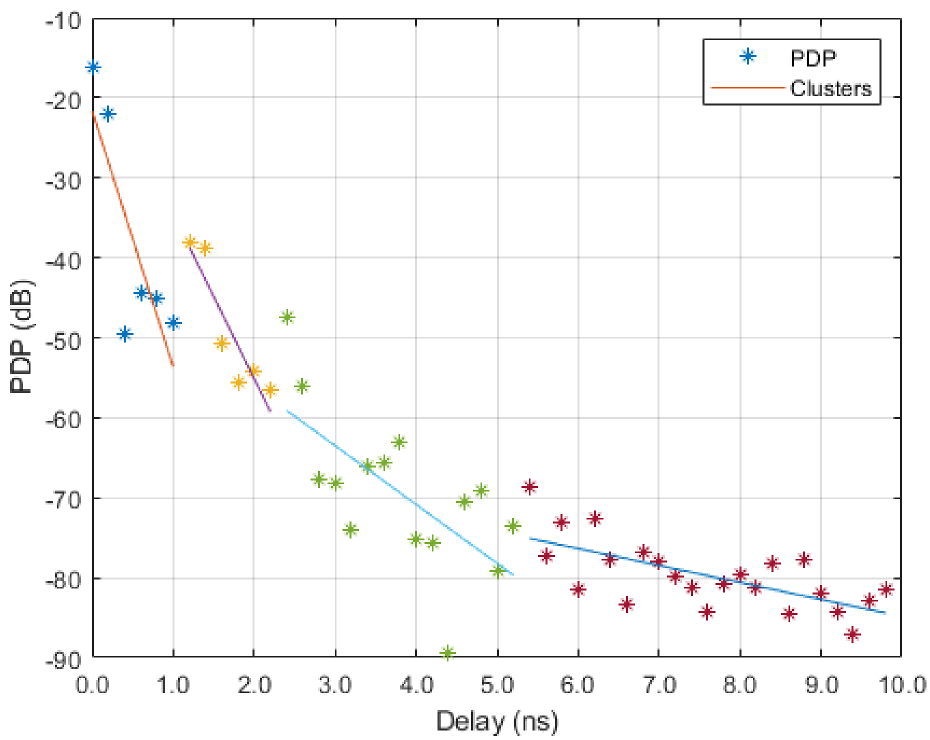

Figure 3.3: A sample PDP in the engine compartment of Fiat Linea MY 2009.

3.2.1 Clustering of PDPs

The determination of the arrival time of each cluster requires an automatic clustering algorithm to identify the change points of the partial slopes of the impulse response. First, we apply Fuzzy C-Means (FCM) clustering, Kernel Power Density (KPD) based clustering and automatic UWB cluster identification algorithms for the clustering of the PDPs to identify their strong and weak characteristics. Then, we develop a novel clustering algorithm based on combining their strong points.

- FCM is a fuzzy clustering algorithm, in which a data point can belong to multiple clusters by assigning membership grades to data points, indicating the degree to which data point belong to each cluster [37]. The membership grades are upgraded after each iteration considering their distance to the cluster heads until it converges to a predefined threshold. A strong aspect of this algorithm is the iterative nature of the algorithm until convergence up to a given accuracy level. However, the number of clusters is predefined in this algorithm, which is a major disadvantage because it is both unfair and impossible to determine the number of clusters through visual inspection. Moreover, an exponentially decreasing trend is expected for rays within the clusters. The main problem with the FCM clustering for our data set is that the cluster heads are determined inaccurately, such that the remaining elements in the cluster outweigh the power of the cluster head, causing positively sloped clusters, resulting in an exponentially increasing trend.
- KPD based clustering algorithm calculates the relative density of each MPC in predefined local neighborhoods and automatically determines the number of clusters based on these relative densities. Next, some of the cluster heads

are merged by comparing their densities to a predefined threshold [38]. The strong aspect of this algorithm is searching for key MPCs in local neighborhoods and merging them within a predefined threshold. The downside of this algorithm is that it was unable to correctly merge cluster heads, which is purely due to the high variance of MPC amplitudes at hand. After the merging of clusters, similar to the problem with FCM algorithm, the remaining elements of the cluster outweigh the cluster head, resulting in several positively sloped clusters.

- An automatic UWB cluster identification is an algorithm that divides the PDP into a predefined number of clusters by ensuring a minimum number of elements in each cluster. The algorithm iteratively continues by updating the number of elements in each cluster and calculating the mean squared error (MSE) of clusters at each iteration, generating all possible clusters at the end. Finally, the iteration with the lowest combined MSE of clusters is selected [39]. The strong aspect of this algorithm is that it ensures the best possible clustering in terms of MSE by analyzing every single combination of clusters. The disadvantage of this algorithm is the same as FCM algorithm, which is the predefined number of clusters. Similar to the previous two algorithms, this algorithm also fails to fulfill the exponentially decreasing trend expectation of clusters in PDPs.

None of the algorithms above was able to ensure all negatively sloped clusters within a PDP condition. However, these three algorithms inspired us to formulate a novel clustering algorithm, which outperforms all of these algorithms, resulting in negatively sloped clusters in all PDPs. The algorithm is given as follows:

- Starting from the rightmost data point, we look for local maximums in small neighborhoods and label those as candidate key MPCs, as inspired from the KPD algorithm. The size of these neighborhoods is the first parameter of the algorithm.
- In order to determine the key MPCs, some of the candidates should be merged within some constraints, just like in KPD algorithm, which divides the merging process into three stages.
    1. We merge consecutive key MPCs that have a distance smaller than a predefined threshold. This threshold is the second parameter of the algorithm.
    2. We merge clusters with positive slopes to either previous or next cluster by comparing average cluster powers to ensure negatively sloped clusters.
    3. We merge clusters with similar slopes that is determined by comparing the difference between their slopes to a predefined threshold, similar to FCM algorithm, which is the third and final parameter of the algorithm.

Every combination of the three parameters that are defined above are tried to cover all the possibilities, as inspired from the automatic UWB cluster identification algorithm. The clustering that ensure negatively sloped clusters in all PDPs along with low MSE is selected for all compartments and each PDP is visually inspected to approve the validity of the algorithm.

3.2.2 Inter-arrival Times of Clusters

The CDF of the inter-arrival times of the clusters for each compartment of a Fiat Linea MY 2009 are shown in Fig. 3.4. The best fitting distribution is observed to be Log-normal distribution, providing a better fit than the exponential distribution, which is originally used in the classical SV model. This is justified by the KS test results with 95% confidence interval: The Log-normal distribution KS test results are 0.1044, 0.0819 and 0.1012, whereas for the Exponential distribution, the KS test results are 0.2482, 0.2752 and 0.2659, which are more than twice of Log-normal test results, for engine compartment, passenger compartment and beneath the chassis, respectively. The Log-normal distribution is given by

$$f_X(x;\mu,\sigma) = \frac{1}{x\sigma\sqrt{2\pi}} \exp\left(\frac{-(lnx - \mu)^2}{2\sigma^2}\right), x > 0 \qquad (3.3)$$

where μ is the mean and σ is the standard deviation parameter of the distribution. Table 3.3 provides the mean and standard deviation of the Log-normal distribution for the inter-arrival times of clusters in all compartments. We observe that there are no drastic changes in terms of mean in between compartments, while the engine compartment has significantly lower variation compared to the other two compartments, due to its relatively smaller space.

Compartment	$\boldsymbol{\mu}$	$\boldsymbol{\sigma}$	$\boldsymbol{KS_{LN}}$	$\boldsymbol{KS_{E}}$
Engine	-20.0546	0.0309	0.1044	0.2482
Passenger	-20.0601	0.6935	0.0819	0.2331
Chassis	-20.0801	0.7846	0.1012	0.2047

Table 3.3: Mean (μ) and standard deviation (σ) parameters of the Log-normal fit for the inter-arrival times of clusters and the KS test results with a 95% confidence interval for Lognormal and Exponential distributions denoted as KS_{LN} and KS_{E}, respectively.

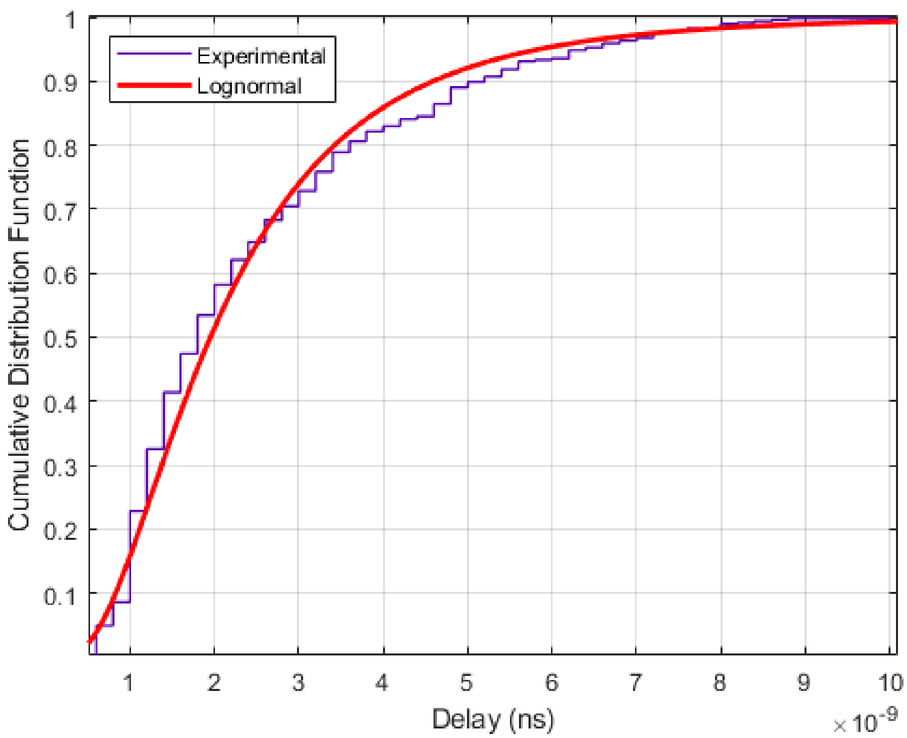
Experimental
Lognormal
Cumulative Distribution Function
0.1
0.2
0.3
0.4
0.5
0.6
0.7
0.8
0.9
1
1
2
3
4
5
6
7
8
9
10
Delay (ns)
$\times 10^{-9}$

(a)

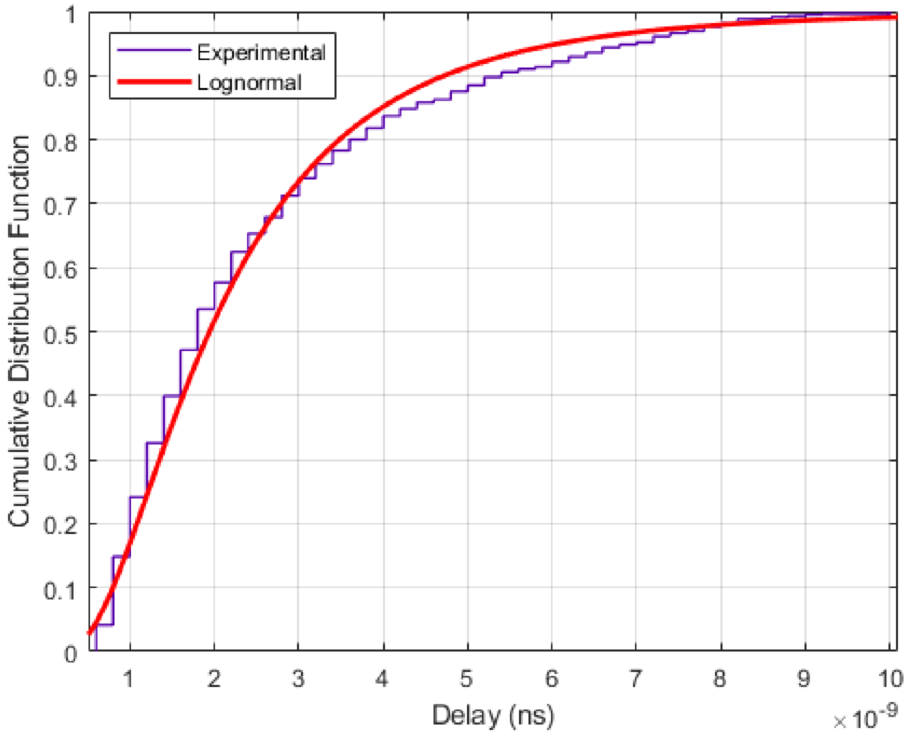
Experimental
Lognormal
Cumulative Distribution Function
Delay (ns)
$\times 10^{-9}$
0
0.1
0.2
0.3
0.4
0.5
0.6
0.7
0.8
0.9
1
1
2
3
4
5
6
7
8
9
10

(b)

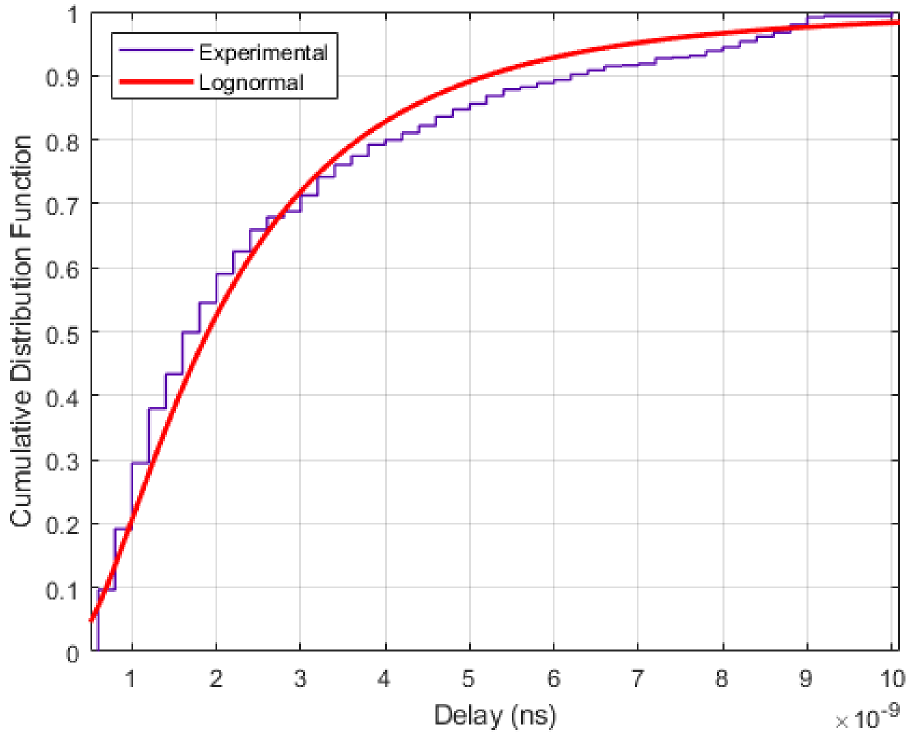

(c)

Figure 3.4: CDF of the inter-arrival times of the clusters for (a) engine compartment, (b) passenger compartment, (c) beneath the chassis.

3.2.3 Cluster - Amplitude Decay Function

The cluster amplitude is defined as the normalized power of the first bin of the cluster by the total energy. The reason for the normalization is to eliminate any dependence on the distance. The dependence of the cluster amplitude on cluster arrival time for each compartment of Fiat Linea MY 2009 is shown in Fig. 3.5. There are no visible data points in the [0- 1] ns range, due to the constraint on the minimum number of elements in a cluster. The propagation delay correction ensures that the first MPC is actually a cluster head. The second cluster cannot start before the first cluster ends, which is restricted due to the condition of the minimum number of elements in a cluster. This gap forms only after the first cluster, because the number of elements in each cluster varies and the following cluster heads cover the delay axis. However, to be able to build a comprehensive simulation model, we need to cover the whole delay axis. Therefore, a dual slope linear model is used to model the cluster-amplitude decay function, as follows:

$$f(T_b) = \begin{cases} c_{11}.T_b + c_{10}, & T_b \leq \tau_{bc} \\ c_{21}.T_b + c_{20}, & T_b > \tau_{bc} \end{cases} \tag{3.4}$$

where $f(T_b)$ is the power of the first bin of the cluster at delay T_b relative to the total energy in dB; τ_{bc} is the breakpoint of two linear fits; c_{11} and c_{10} are the slope of the fit and the cluster amplitude axis intercept point of the fit before the breakpoint, respectively; c_{21} and c_{20} are the slope of the fit and the cluster amplitude axis intercept point of the fit after the breakpoint, respectively. The parameters of the dual slope linear fit model for cluster amplitude decay function for all three compartments are given in Table 3.4. It is observed that there are slight changes in these parameters across different compartments, which is expected due to the completely different physical structures of each compartment, i.e., dense shadowing objects at various distances in the engine compartment, and unique distributions of line-of-sight (LoS) and NLoS transmitter and receiver links in the compartments.

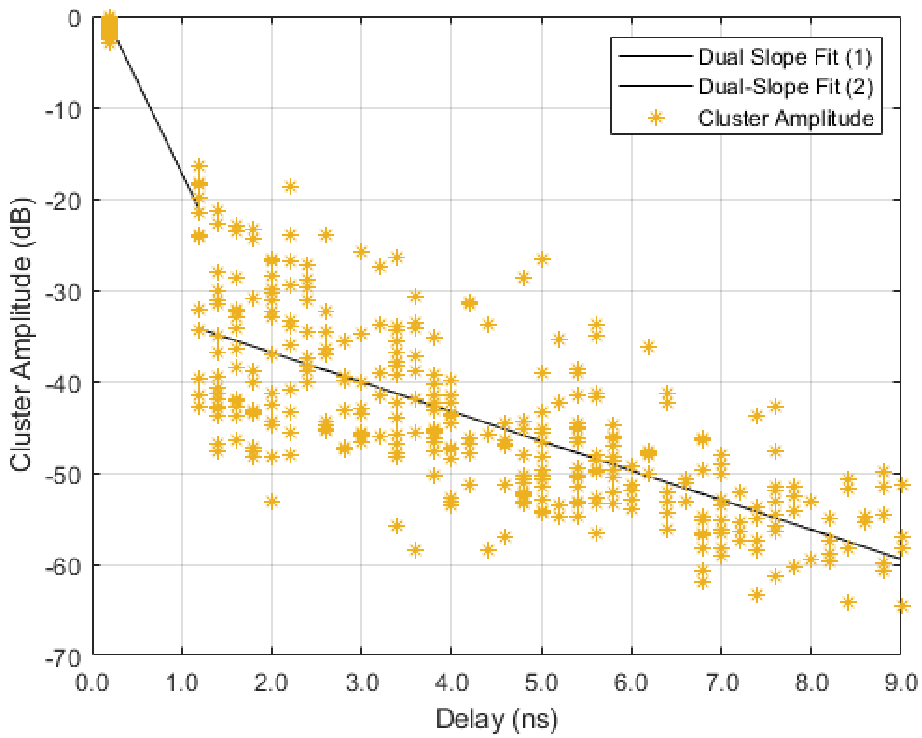
Dual Slope Fit (1)
Dual-Slope Fit (2)
Cluster Amplitude
Cluster Amplitude (dB)
0
-10
-20
-30
-40
-50
-60
-70
0.0
1.0
2.0
3.0
4.0
5.0
6.0
7.0
8.0
9.0
Delay (ns)

(a)

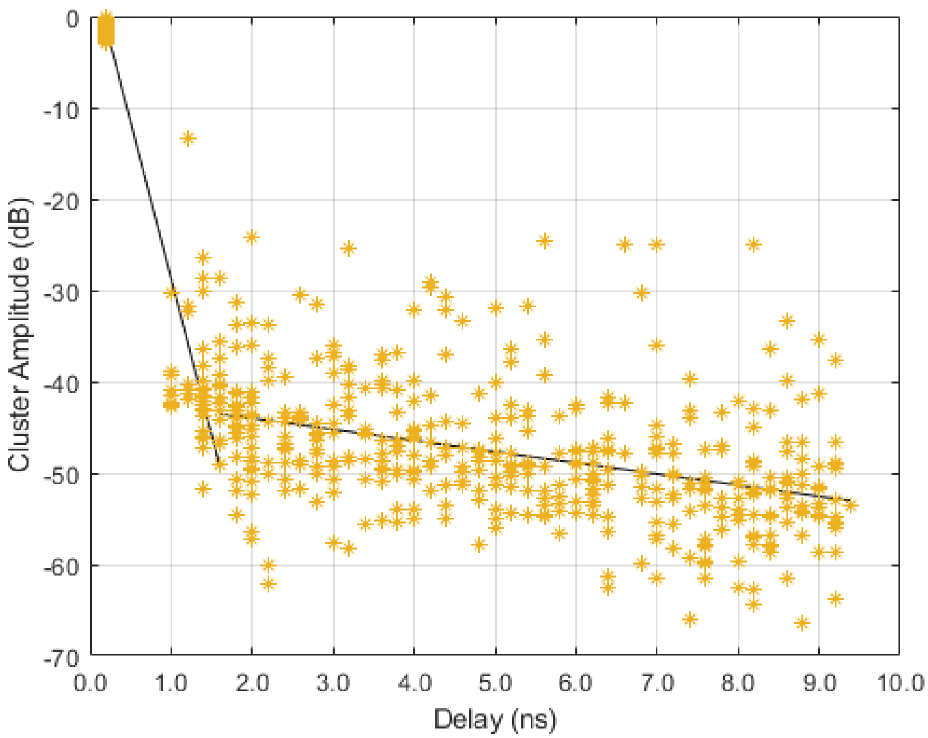

Cluster Amplitude (dB)
0
-10
-20
-30
-40
-50
-60
-70
0.0
1.0
2.0
3.0
4.0
5.0
6.0
7.0
8.0
9.0
10.0
Delay (ns)

(b)

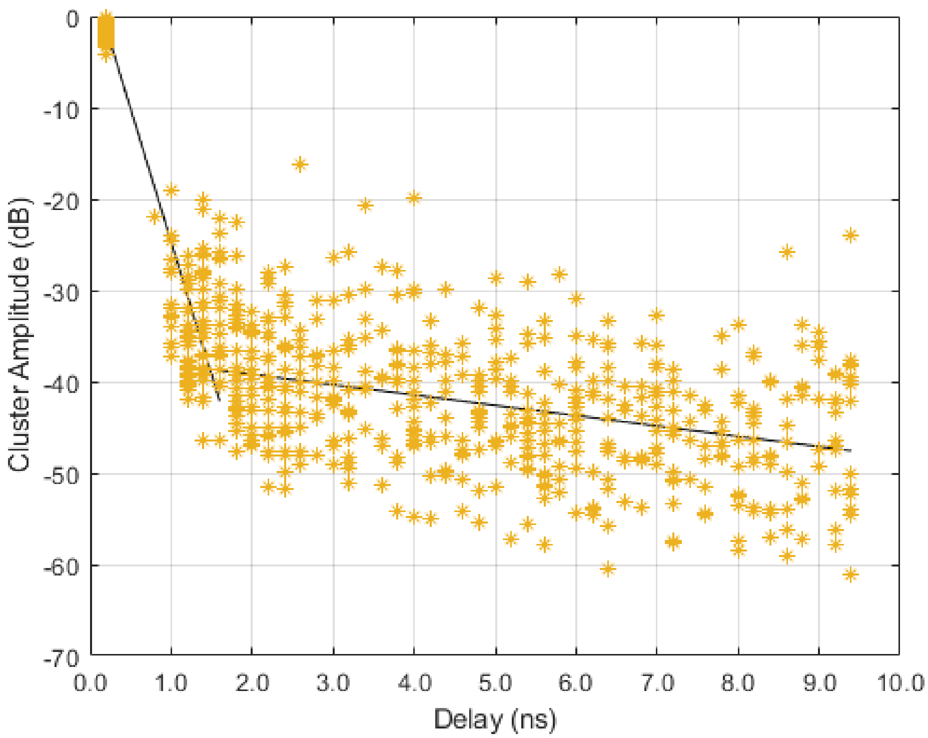

(c)

Figure 3.5: Dependence of the cluster amplitude on the arrival time for (a) engine compartment, (b) passenger compartment, (c) beneath the chassis.

Scenario	c_{11}	c_{10}	c_{21}	c_{20}	τ_{bc}
Engine	-20.319	3.1162	-3.2316	-30.3779	1.2
Passenger	-34.263	5.5454	-1.2206	-41.5632	1.6
Chassis	-29.101	4.3997	-1.1296	-36.9419	1.6

Table 3.4: Cluster amplitude function parameters. The units of c_{11} and c_{21} are dB/ns, $c_{10}$and c_{20} dB and τ_{bc} is ns.

3.2.4 Ray - Amplitude Decay Function

In the previous section, the power of the first bin of all the clusters are calculated. In order to calculate the power of all the bins in these clusters, the ray decay rates of clusters need to be determined. Given that the ray decay rates are linear, which can be seen in Fig. 3.3, the power of the ath bin in the bth cluster is formulated as;

$$g\left(T_b + \tau_{b,a}\right) = f(T_b) - \xi(T_b)\tau_{b,a} \tag{3.5}$$

where $\xi(T_b)$ is the ray decay rate of the cluster at delay T_b in dB-scale and $\tau_{b,a}$ is the delay of the ath multipath component in the bth cluster relative to the bth cluster arrival time T_b.

The dependence of the ray amplitude decay on the arrival time T_b is given in Fig. 3.6. Similar to cluster-amplitude decay function, there are no visible data points in the [0-1] ns range. This is due to the exact same reason as explained in the previous section: The minimum number of clusters in the first cluster of the PDP causes the earliest upcoming cluster to start after a gap. Once again, a comprehensive simulation model requires the ray decay rate function to cover the whole delay axis. Therefore, the ray-amplitude decay function is also modeled by the dual slope linear model, which is;

$$\xi(T_b) = \begin{cases} d_{11}.T_b + d_{10},\ T_b \leq\ \tau_{br} \\ \\ d_{21}.T_b + d_{20},\ T_b >\ \tau_{br} \end{cases} \tag{3.6}$$

where τbr is the breakpoint of two linear fits; d_{11} and d_{10} are the slope of the fit and the ray decay rate axis intercept point of the fit before the breakpoint, respectively;

d_{21} and d_{20} are the slope of the fit and the ray decay rate axis intercept point of the fit after the breakpoint, respectively. The parameters of dual slope linear fit model for ray amplitude decay rate function for all three compartments are given in Table 3.5. It is observed that there are major differences between the engine compartment and the other two compartments, which is expected due to the vast number of shadowing objects being stacked in a relatively smaller area than other compartments in the engine compartment.

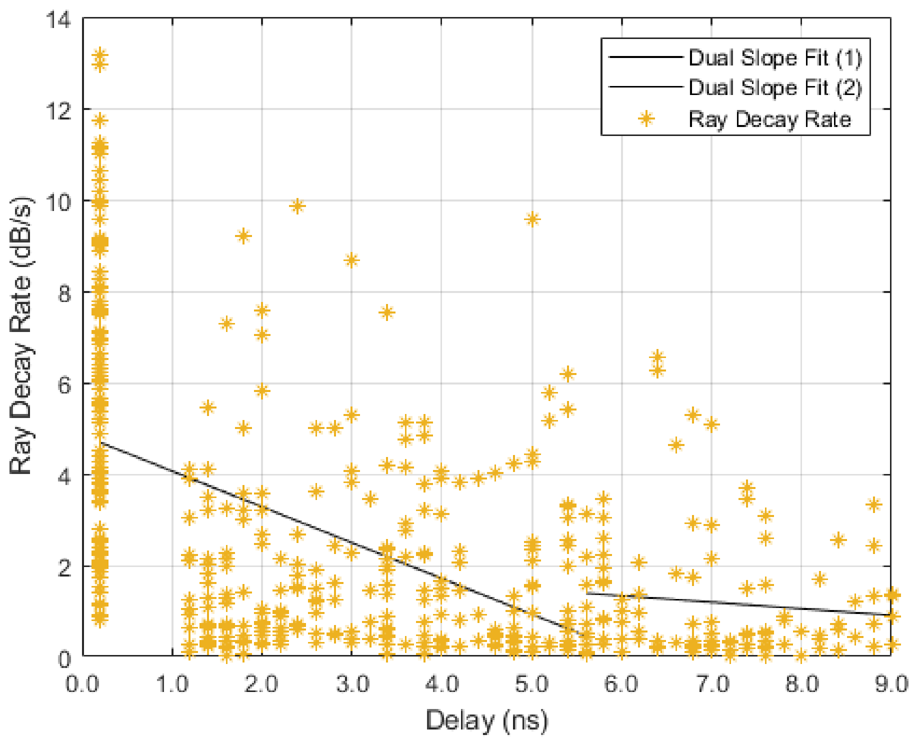
Dual Slope Fit (1)
Dual Slope Fit (2)
Ray Decay Rate
Ray Decay Rate (dB/s)
Delay (ns)
0
2
4
6
8
10
12
14
0.0
1.0
2.0
3.0
4.0
5.0
6.0
7.0
8.0
9.0

(a)

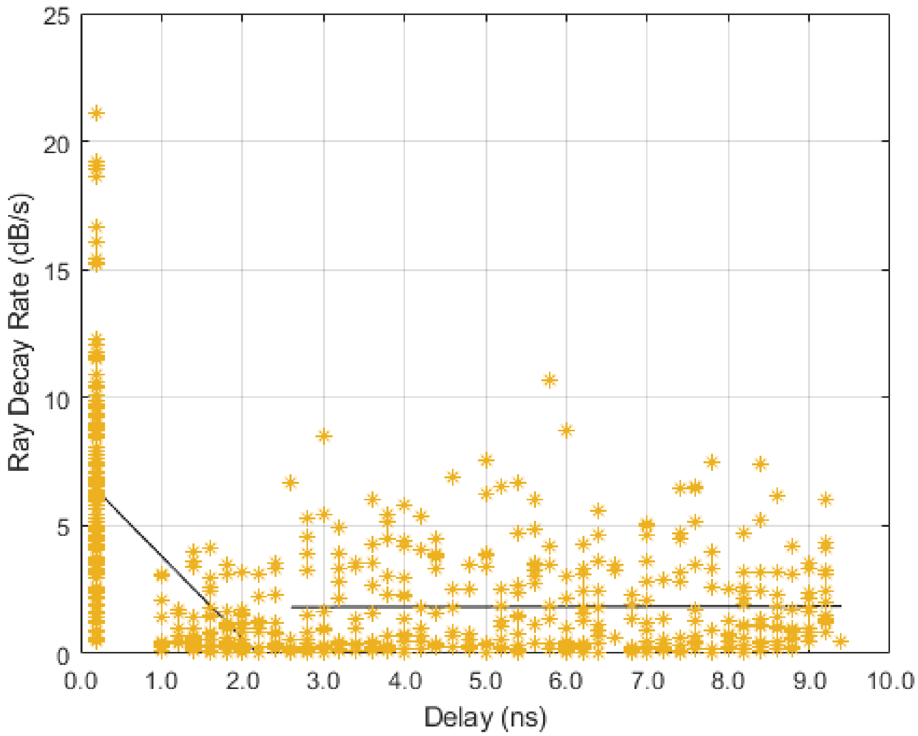
25
20
15
10
5
0
Ray Decay Rate (dB/s)
0.0
1.0
2.0
3.0
4.0
5.0
6.0
7.0
8.0
9.0
10.0
Delay (ns)

(b)

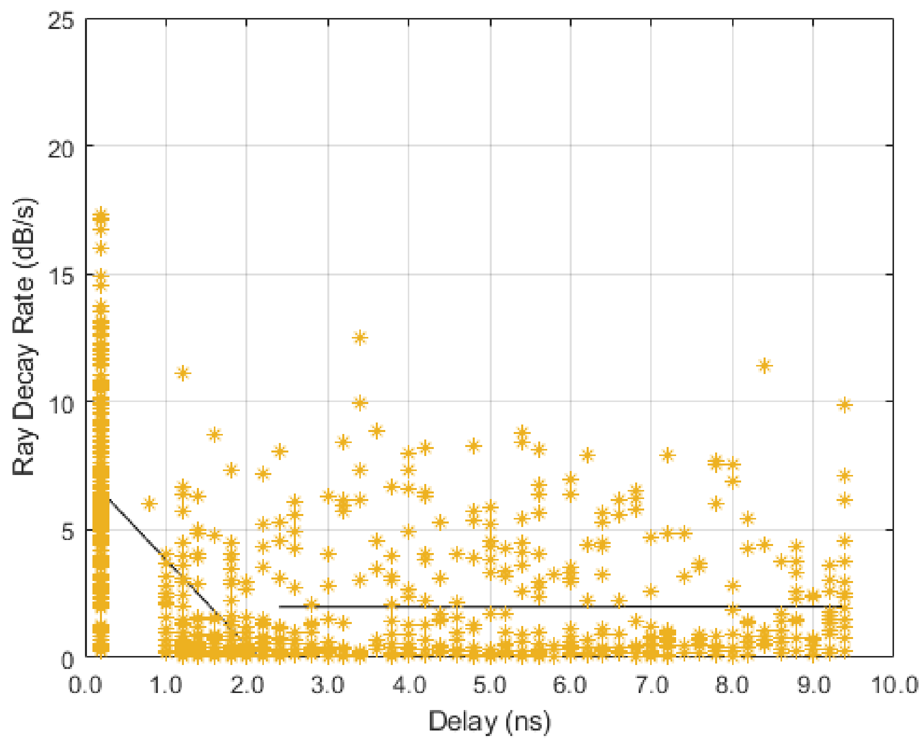

(c)

Figure 3.6: Dependence of the ray decay rate on the arrival time for (a) engine compartment, (b) passenger compartment, (c) beneath the chassis.

Scenario	d_{11}	d_{10}	d_{21}	d_{20}	τ_{br}
Engine	-0.7837	4.8443	-14.201	2.1850	5.6
Passenger	-3.2087	7.0141	4678.4	1.8030	2.6
Chassis	-3.3491	7.1731	1401.5	1.9814	2.4

Table 3.5: Ray amplitude decay function parameters. The units of d_{11} and $d_{21}$are dB/ns, d_{10} and d_{20} dB and τ_{br} is ns.

3.3 Variation of PDP Around SV Model

Although the clustered channel impulse response is built by using the SV model, as shown in Fig. 3.3, the actual channel impulse response varies around this SV model. The best fits for the variations in each delay bin are analyzed to have a better understanding of the distribution of these variations. KS test results within 95% confidence interval for Normal and Rayleigh distributions are given in Fig. 3.7. Normal distribution is by far the best distribution in all of the delay bins considering all three compartments. The mean and standard deviation of the normal distribution in all delay bins for all compartments are given in Fig. 3.8. The mean and standard deviation are independent of the delay, except the first delay bin. The main reason is the large ray decay rate of the first bin with the number of elements in the cluster close to the minimum threshold, causing large variations. The SV model accurately represents the PDP measurements as the average of the mean values over all delay bins is 0, as shown by μz in Table 3.6. Moreover, the average of the standard deviation values over all delay bins, denoted by σz in Table 3.6, are also very similar among all compartments. This demonstrates that the variation of the experimental PDP around the SV model is not only independent of delay bin but also independent of vehicular compartment.

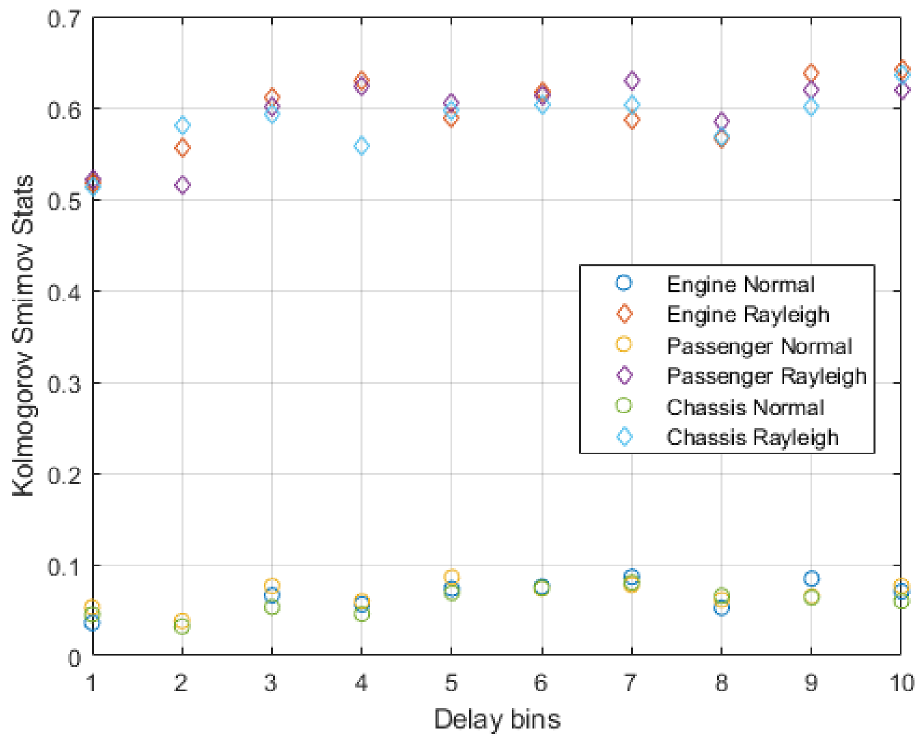

Figure 3.7: KS test results with 95% confidence interval for the difference between experimental PDPs and SV model in each delay bin for all three compartments.

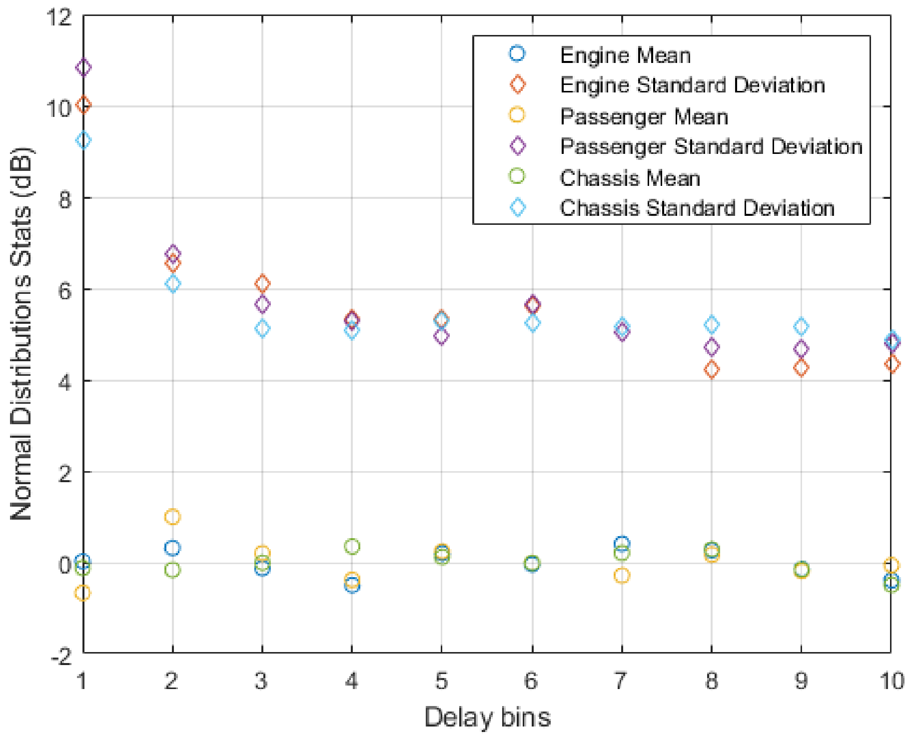

Figure 3.8: Normal distribution statistics of the difference between experimental PDPs and the SV model in each delay bin for all three compartments

Scenario	μ_z	σ_z
Engine	0	5.8223
Passenger	0	5.8340
Chassis	0	5.6574

Table 3.6: Average mean and standard deviation of variation of experimental PDP around SV Model.

Chapter 4: Channel Model Implementation

4.1 Generation of Statistical Channel Model

In order to generate the PDP of a transmitter and receiver pair with only the distance between them as input, a very similar algorithm to the one studied in [8] is used. The detailed explanation of the pseudo code, provided in Fig. 4.1, is as follows:

- The results derived in Section 3.2.2 are utilized to determine the cluster head arrival times. The first cluster head's arrival time is defined as $T_0 = d/c$, where d is the distance between a transmitter and receiver pair and c is the speed of light (Line 1). The arrival times of succeeding cluster heads, T_B, are determined by using the Log-normal distribution with specifications given in Table 3.1 (Line 4). This process is repeated until the arrival time, T_B, attains the maximum delay spread, which is 10 ns (Line 3).
- The results derived in Section 3.2.3 are utilized to determine the dependence of the cluster amplitude on the arrival time (Line 9). Due to the fact that propagation delay is excluded from the PDP, the dual slope linear model given in Eqn. (3.4) with specifications given in Table 3.4 is evaluated at $T_b - T_0$ for $b = [0, B - 1]$.
- The results derived in Section 3.2.4 are utilized to determine the power of the succeeding bins of the cluster (Line 10). The power of the ath bin of the bth cluster is computed by using the ray decay rate function formulated in Eqns.

(3.5) and (3.6) with specifications given in Table 3.5. Up to this point, the general shape of the channel impulse response is formed.

- The results derived in Section 3.1 are utilized to scale the PDP at hand with the path loss model given in Eqn. (3.1) with specifications given in Table 3.1 (Line 13).
- The results derived in Section 3.3 are utilized to add random variations of experimental PDPs around the SV model to each delay bin (Line 14). The output of the simulation model, which is the resulting PDP, is calculated by adding the normal random variable with specifications given in Table 3.6 to every delay bin of the PDP.

Algorithm 1 Simulation Model
Input: Distance between Tx and Rx
Output: PDP between Tx and Rx

$T_0 = d/c$;
$B = 0$;
while $T_B \leq$ Delay Spread **do**
    $T_{B+1} = T_B + Lognormal(\mu, \sigma)$;
    $B = B + 1$;
end while
for $b = 0 : (B - 1)$ **do**
    for $\tau_{b,a} = 0 : T_{b+1} - T_b - 1$ **do**
        Find $f(T_b - T_0)$;
        Find $g(T_b - T_0) = f(T_b - T_0) - \zeta(T_b - T_0)\tau_{b,a}$;
    end for
end for
Scale PDP with path loss;
Add $N(0, \sigma_z^2)$ to each delay bin of PDP;

Figure 4.1: Pseudocode for the simulation algorithm.

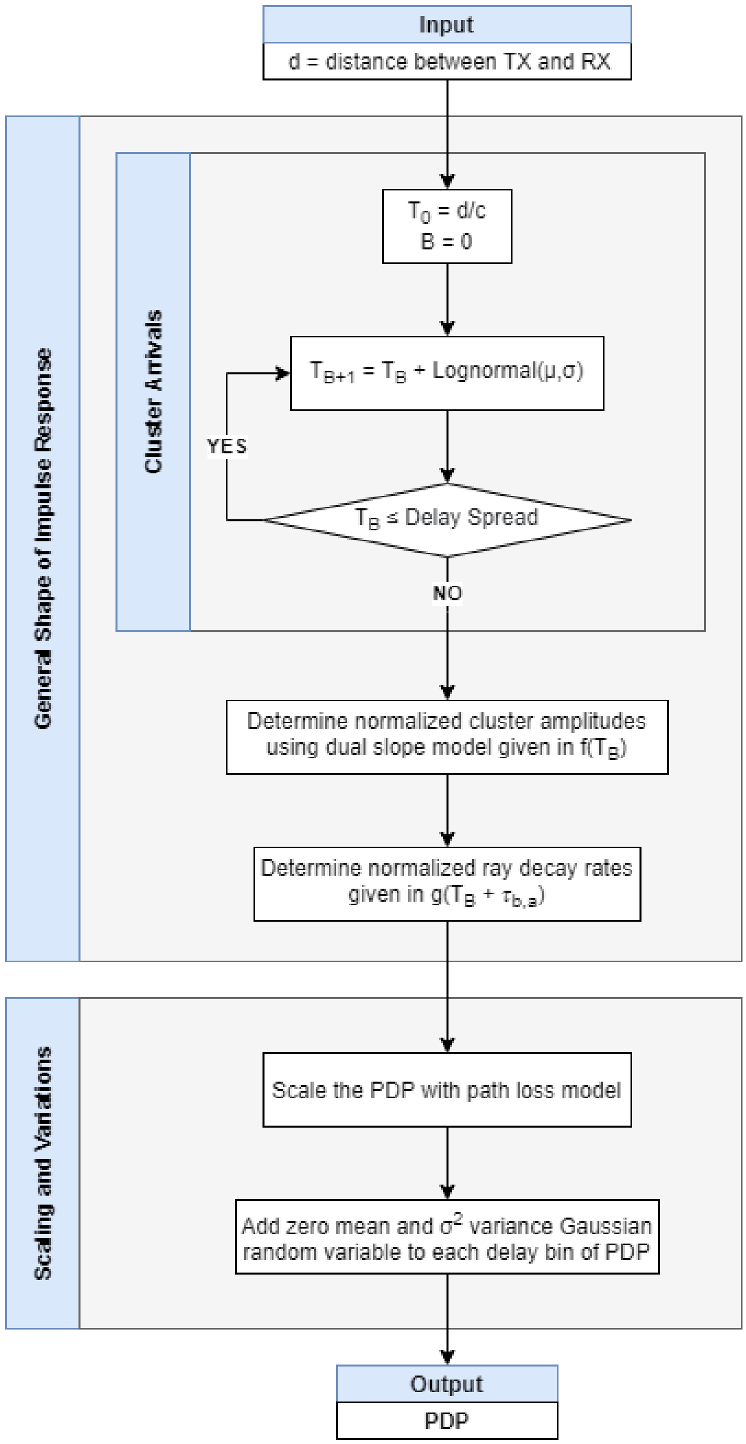

Figure 4.2: Flowchart for the simulation algorithm.

4.2 Validation of Simulation Model

The simulation model described in the previous subsection is implemented in MATLAB R2020b for engine compartment, passenger compartment and beneath the chassis. The validation of the simulation model is done by comparing the experimental and simulated CDFs of received energy and RMS delay spread. The CDF of the received power for both experimental and simulated PDPs are given in Fig. 4.3 for all three compartments. Experimental and simulated PDPs are observed to be coherent considering their received powers with KS test results within 95% confidence interval as 0.211, 0.269 and 0.229 for engine compartment, passenger compartment and beneath the chassis, respectively.

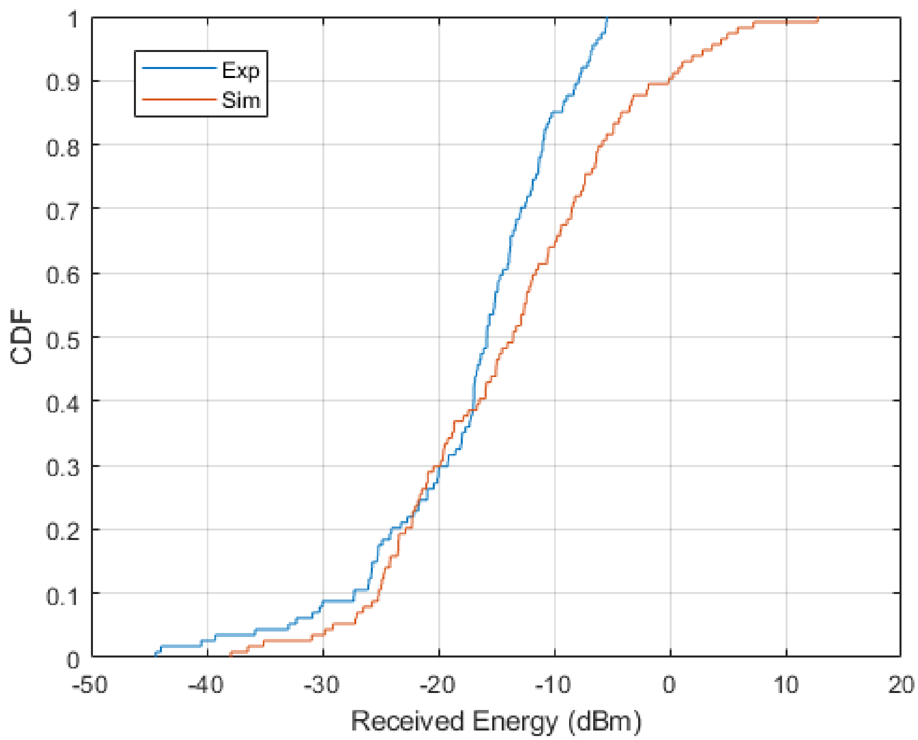
Exp
Sim
CDF
Received Energy (dBm)
1
0.9
0.8
0.7
0.6
0.5
0.4
0.3
0.2
0.1
0
-50
-40
-30
-20
-10
0
10
20

(a)

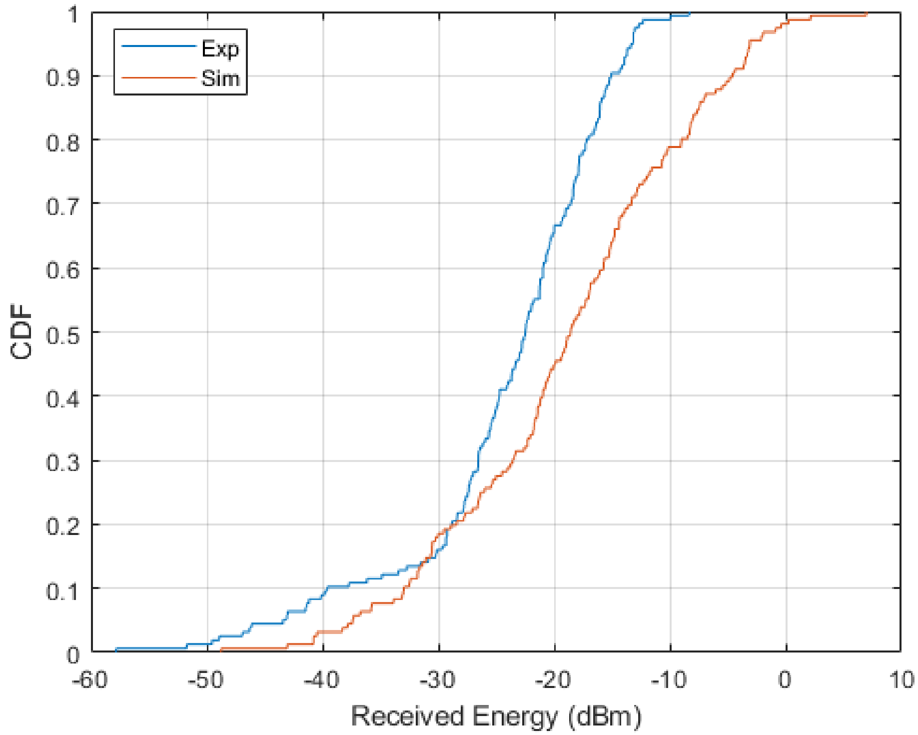
Exp
Sim
CDF
0
0.1
0.2
0.3
0.4
0.5
0.6
0.7
0.8
0.9
1
-60
-50
-40
-30
-20
-10
0
10
Received Energy (dBm)

(b)

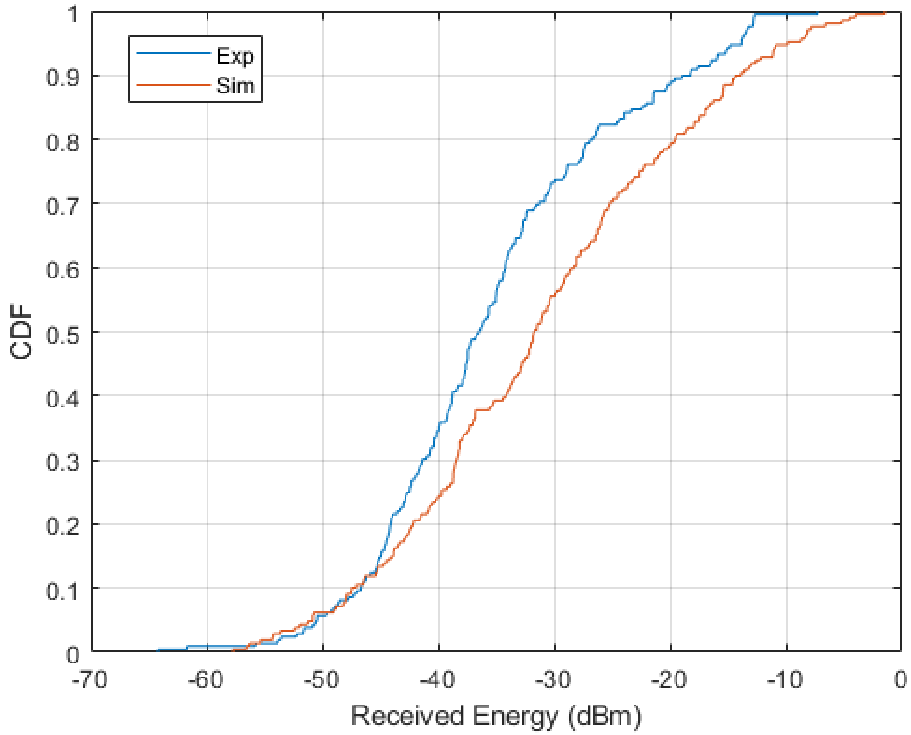

(c)

Figure 4.3: CDF of the received power of experimental and simulated PDPs for (a) engine compartment, (b) passenger compartment, (c) beneath the chassis.

The CDF of the RMS delay spread for both experimental and simulated PDPs are given in Fig. 4.4 for all three compartments. Considering their RMS delay spread, the experimental PDPs are wider than those of the simulated PDPs with KS test results within 95% confidence interval as 0.395, 0.147 and 0.124 for engine compartment, passenger compartment and beneath the chassis, respectively. Although there were large amounts of variations around the model and there was a gap in [0-1] ns range in Figs. 6 and 7, we represented the dependence of cluster amplitude and ray decay rate on cluster arrival time with dual slope linear models. This approximation might be causing this disagreement in experimental and simulated PDPs.

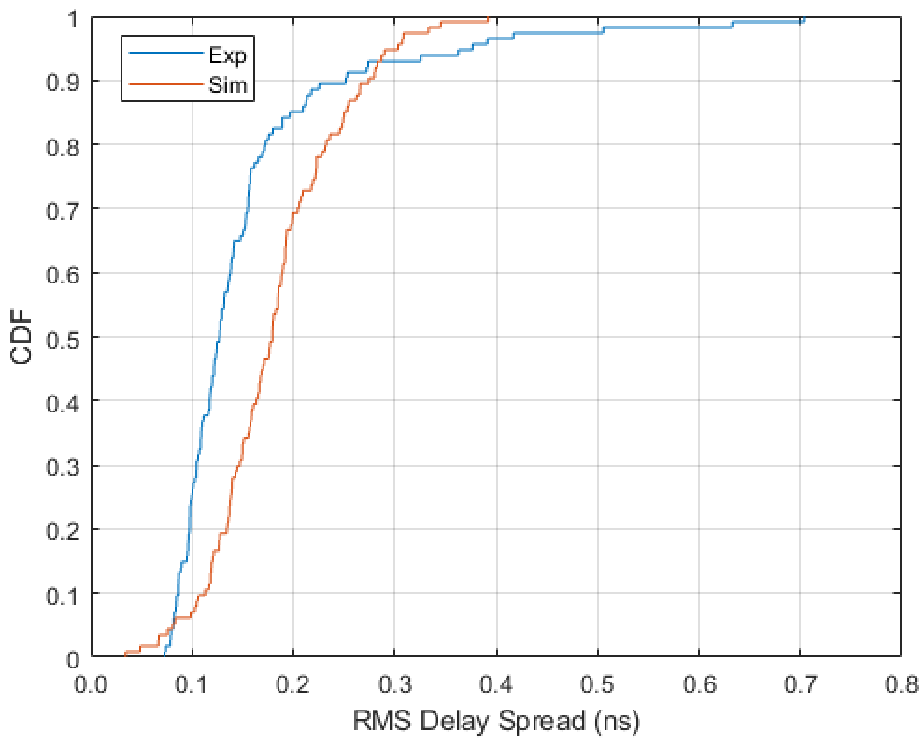
Exp
Sim
CDF
1
0.9
0.8
0.7
0.6
0.5
0.4
0.3
0.2
0.1
0
0.0
0.1
0.2
0.3
0.4
0.5
0.6
0.7
0.8
RMS Delay Spread (ns)

(a)

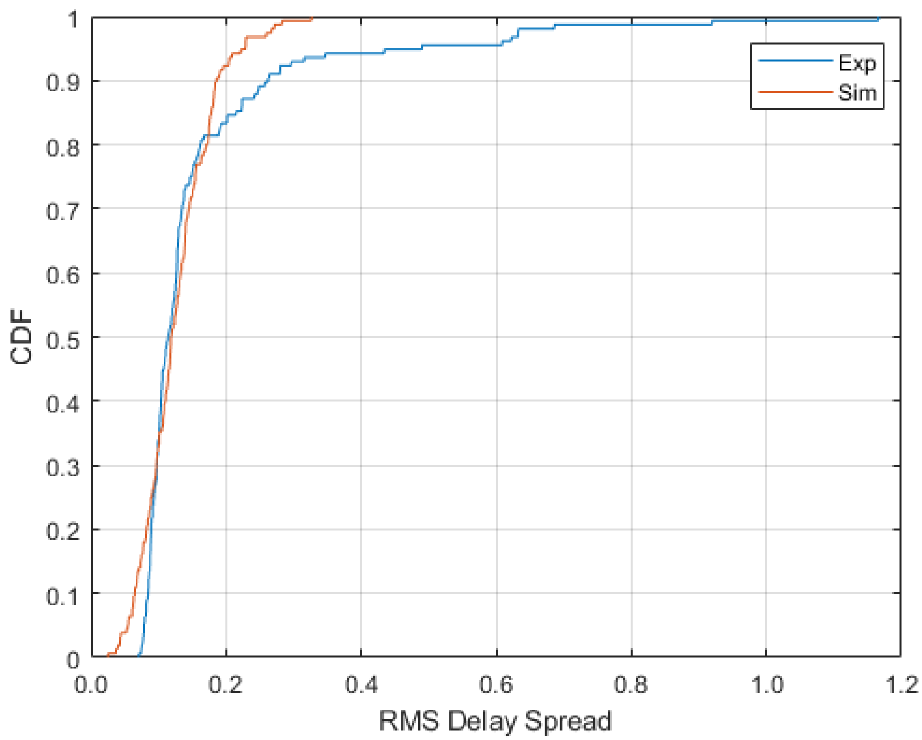
1
0.9
0.8
0.7
0.6
0.5
0.4
0.3
0.2
0.1
0
CDF
0.0
0.2
0.4
0.6
0.8
1.0
1.2
RMS Delay Spread
Exp
Sim

(b)

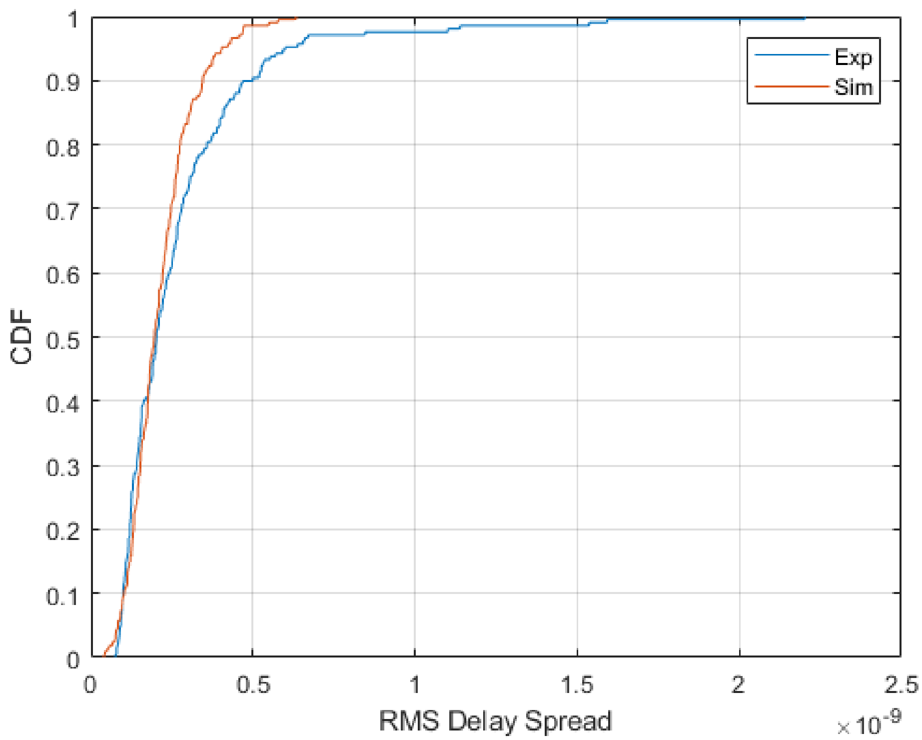

(c)

Figure 4.4: CDF of RMS delay spread of the experimental and simulated PDPs for (a) engine compartment, (b) passenger compartment, (c) beneath the chassis.

Chapter 5: Conclusion

In this thesis, the mmWave channel model for IVWSNs is derived based on a vast number of measurement data for 14x14, 13x13 and 15x15 transmitter and receiver links in engine compartment, passenger compartment and beneath the chassis, respectively. In order to build an accurate simulation model for the mmWave channel, we derived path loss model, variation of experimental data around the path loss model, distribution of the inter-arrival times of clusters, the dependencies of the cluster amplitudes and ray decay rates on the cluster arrival times, and distribution of the variations of experimental PDPs around the SV model. The simulation model is generated for all three compartments and validated by comparing the distributions of received power and RMS delay spread of experimental and simulated PDPs. The key results of this work can be highlighted as follows:

- The path loss exponent of the engine compartment, passenger compartment and beneath the chassis is approximately 3, meaning all three compartments have similar characteristics considering the path loss.
- The power variation around the SV model, which is the best fit line on path loss, is represented with a GEV distribution with zero mean for all compartments. The standard deviation for the engine compartment is 5 dB, which is lower than that of passenger compartment and beneath the chassis, which are 7.5 and 7.7 dB, respectively. This is probably due to the fact that the engine compartment is relatively a smaller compartment and the variations are smaller in magnitude.

- A modified SV model is a good representation of the clustering of PDPs. The distribution of the inter-arrival times of the clusters are modeled by using a Log-normal fit. The dependencies of the cluster amplitude and ray decay rate on cluster arrival time are modeled by using dual slope linear fit model with breakpoints at 1.2 ns and 5.6 ns, respectively, for engine compartment, and 1.6 ns and 2.6 ns, respectively, for the other two compartments. The difference between the engine compartment and the other two compartments are due to the dense shadowing objects being clustered in a small space inside the engine compartment.
- The experimental PDPs vary around the SV model and this variation is represented by normal random variable with zero mean and 5.8 dB standard deviation for all three compartments. These values are independent of both the delay bins and the compartment of vehicle. The representation of variations having almost no changes in between compartments supports the reliability of the simulation model built over vast number of measurements.

References

[1] N. Navet, Y. Song, F. Simonot-Lion, and C. Wilwert, "Trends in automotive communication systems," Proceedings of the IEEE, vol. 93, no. 6, pp. 1204–1223, 2005.

[2] N. Navet and F. Simonot-Lion, "In-vehicle communication networks-a historical perspective and review," tech. rep., University of Luxembourg, August 2013.

[3] S. C. Ergen, A. Sangiovanni-Vincentelli, X. Sun, R. Tebano, S. Alalusi, G. Audisio, and M. Sabatini, "The tire as an intelligent sensor," IEEE Transactions on Computer-Aided Design of Integrated Circuits and Systems, vol. 28, no. 7, pp. 941–955, 2009.

[4] A. R. Moghimi, H. Tsai, C. U. Saraydar, and O. K. Tonguz, "Characterizing intra-car wireless channels," IEEE Transactions on Vehicular Technology, vol. 58, no. 9, pp. 5299–5305, 2009.

[5] H. Tsai, O. K. Tonguz, C. Saraydar, T. Talty, M. Ames, and A. Macdonald, "Zigbee-based intra-car wireless sensor networks: a case study," IEEE Wireless Communications, vol. 14, pp. 67–77, December 2007.

[6] O. K. Tonguz, H. Tsai, C. Saraydar, T. Talty, and A. Macdonald, "Intracar wireless sensor networks using rfid: Opportunities and challenges," in 2007 Mobile Networking for Vehicular Environments, pp. 43–48, May 2007.

[7] C. U. Bas and S. C. Ergen, "Ultra-wideband channel model for intravehicular wireless sensor networks," in 2012 IEEE Wireless Communications and Networking Conference (WCNC), pp. 42–47, 2012.

[8] U. Demir, C. U. Bas, and S. Coleri Ergen, "Engine compartment uwb channel model for intravehicular wireless sensor networks," IEEE Transactions on Vehicular Technology, vol. 63, no. 6, pp. 2497–2505, 2014.

[9] C. U. Bas and S. C. Ergen, "Ultra-wideband channel model for intravehicular wireless sensor networks beneath the chassis: From statistical model to simulations," IEEE Transactions on Vehicular Technology, vol. 62, no. 1, pp. 14–25, 2013.

[10] U. Demir and S. Coleri Ergen, "Arima-based time variation model for beneath the chassis uwb channel," EURASIP Journal on Wireless Communications and Networking, vol. 2016, 08 2016.

[11] A. Chandra, A. Prokes, T. Mikul ˇ a´sek, J. Blumenstein, P. Kukolev, ˇ T. Zemen, and C. F. Mecklenbrauker, "Frequency-domain in-vehicle ¨ uwb channel modeling," IEEE Transactions on Vehicular Technology, vol. 65, pp. 3929–3940, June 2016.

[12] J. Li and T. Talty, "Channel characterization for ultra-wideband intravehicle sensor networks," in MILCOM 2006 - 2006 IEEE Military Communications conference, pp. 1–5, 2006.

[13] T. Tsuboi, J. Yamada, N. Yamauchi, M. Nakagawa, and T. Maruyama, "Uwb radio propagation inside vehicle environments," in 2007 7th International Conference on ITS Telecommunications, pp. 1–5, 2007.

[14] P. C. Richardson, Weidong Xiang, and W. Stark, "Modeling of ultrawideband channels within vehicles," IEEE Journal on Selected Areas in Communications, vol. 24, no. 4, pp. 906–912, 2006.

[15] J. Blumenstein, A. Prokes, A. Chandra, T. Mikulasek, R. Marsalek, T. Zemen, and C. Mecklenbrauker, "In-vehicle channel measurement, ¨ characterization, and spatial consistency comparison of 30–11 GHz and 55–65 GHz frequency bands," IEEE Transactions on Vehicular Technology, vol. 66, pp. 3526–3537, May 2017.

[16] M. Schack, M. Jacob, and T. Kiirner, "Comparison of in-car uwb and 60 ghz channel measurements," in Proceedings of the Fourth European Conference on Antennas and Propagation, pp. 1–5, April 2010.

[17] R. Nakamura and A. Kajiwara, "Empirical study on 60ghz in-vehicle radio channel," in 2012 IEEE Radio and Wireless Symposium, pp. 327– 330, 2012.

[18] M. Koca, G. Gurbilek, B. Soner, and S. Coleri, “Empirical feasibility analysis for energy harvesting intravehicular wireless sensor networks,” IEEE Internet of Things Journal, vol. 8, no. 1, pp. 179–186, 2021.

[19] S. Ju, Y. Xing, O. Kanhere, and T. S. Rappaport, “3-d statistical indoor channel model for millimeter-wave and sub-terahertz bands,” 2020.

[20] L. Feng, H. Yang, R. Q. Hu, and J. Wang, “Mmwave and vlcbased indoor channel models in 5g wireless networks,” IEEE Wireless Communications, vol. 25, no. 5, pp. 70–77, 2018.

[21] X. Wu, C. Wang, J. Sun, J. Huang, R. Feng, Y. Yang, and X. Ge, “60- ghz millimeter-wave channel measurements and modeling for indoor office environments,” IEEE Transactions on Antennas and Propagation, vol. 65, no. 4, pp. 1912–1924, 2017.

[22] I. A. Hemadeh, K. Satyanarayana, M. El-Hajjar, and L. Hanzo, “Millimeter-wave communications: Physical channel models, design considerations, antenna constructions, and link-budget,” IEEE Communications Surveys Tutorials, vol. 20, no. 2, pp. 870–913, 2018.

[23] S. H. A. Momo and M. M. Mowla, “Statistical analysis of an outdoor mmwave channel model at 73 ghz for 5g networks,” in 2019 International Conference on Computer, Communication, Chemical, Materials and Electronic Engineering (IC4ME2), pp. 1–4, 2019.

[24] M. R. Akdeniz, Y. Liu, M. K. Samimi, S. Sun, S. Rangan, T. S. Rappaport, and E. Erkip, “Millimeter wave channel modeling and cellular capacity evaluation,” IEEE Journal on Selected Areas in Communications, vol. 32, no. 6, pp. 1164–1179, 2014.

[25] A. U. Rahman, U. Ghosh, A. Chandra, and A. Prokes, “Channel modelling for 60ghz mmwave communication inside bus,” in 2018 IEEE Vehicular Networking Conference (VNC), pp. 1–6, 2018.

[26] A. Chandra, P. Kukolev, T. Mikulasek, and A. Prokes, “Frequencydomain in-vehicle channel modelling in mmw band,” 09 2015.

[27] J. Blumenstein, T. Mikulasek, T. Zemen, C. Mecklenbraeuker, R. Marsalek, and A. Proke, “In-vehicle mm-wave channel model ´ and measurement,” 2014 IEEE 80th Vehicular Technology Conference (VTC2014-Fall), pp. 1–5, 2014.

[28] J. Moreno Garcia Loygorri, C. Briso-Rodr´ıguez, I. Arnedo, C. CalvoRamirez, M. Laso, D. He, F. Jimenez, and V. Gonzalez, “Wideband ´ channel modeling for mm-wave inside trains for 5g-related applications,” Wireless Communications and Mobile Computing, vol. 2018, pp. 1–11, 04 2018.

[29] B. De Beelde, E. Tanghe, M. Yusuf, D. Plets, E. De Poorter, and W. Joseph, “60 ghz path loss modelling inside ships,” in 2020 14th European Conference on Antennas and Propagation (EuCAP), pp. 1–5, 2020.

[30] Y. Wang, S. Mao, and T. S. Rappaport, “On directional neighbor discovery in mmwave networks,” in 2017 IEEE 37th International Conference on Distributed Computing Systems (ICDCS), pp. 1704–1713, 2017.

[31] O. Kanhere and T. S. Rappaport, “Position locationing for millimeter wave systems,” in 2018 IEEE Global Communications Conference (GLOBECOM), pp. 206–212, 2018.

[32] D. Munoz, F. Bouchereau, C. Vargas, and R. Enriquez, “Chapter 2 - signal parameter estimation for the localization problem,” in Position Location Techniques and Applications (D. Munoz, F. Bouchereau, C. Vargas, and R. Enriquez, eds.), pp. 23 – 65, Oxford: Academic Press, 2009.

[33] G. R. MacCartney, Junhong Zhang, Shuai Nie, and T. S. Rappaport, “Path loss models for 5g millimeter wave propagation channels in urban microcells,” in 2013 IEEE Global Communications Conference (GLOBECOM), pp. 3948–3953, 2013.

[34] A. Al-Hourani, S. Chandrasekharan, and S. Kandeepan, “Path loss study for millimeter wave device-to-device communications in urban environment,” in 2014 IEEE International Conference on Communications Workshops (ICC), pp. 102–107, 2014.

[35] L. Ahumada, A. Angles, E. Carre ` no, and D. Schkolnik, “Modeling ˜ shadow fading correlation in 60 ghz outdoor urban street canyons,” in 2017 IEEE-APS

Topical Conference on Antennas and Propagation in Wireless Communications (APWC), pp. 193–196, 2017.

[36] A. A. M. Saleh and R. Valenzuela, “A statistical model for indoor multipath propagation,” IEEE Journal on Selected Areas in Communications, vol. 5, no. 2, pp. 128–137, 1987.

[37] Z. Huang, R. Zhang, J. Pan, Y. Jiang, and D. Zhai, “A framework of multipath clustering based on space-transformed fuzzy c -means and data fusion for radio channel modeling,” IEEE Transactions on Vehicular Technology, vol. PP, pp. 1–1, 10 2019.

[38] R. He, Q. Li, B. Ai, Y. L. Geng, A. F. Molisch, V. Kristem, Z. Zhong, and J. Yu, “A kernel-power-density-based algorithm for channel multipath components clustering,” IEEE Transactions on Wireless Communications, vol. 16, no. 11, pp. 7138–7151, 2017.

[39] M. Corrigan, A. Walton, Weihong Niu, Jia Li, and T. Talty, “Automatic uwb clusters identification,” in 2009 IEEE Radio and Wireless Symposium, pp. 376–379, 2009.